

Targeted T_1 Magnetic Resonance Imaging Contrast Enhancement with Extraordinarily Small CoFe_2O_4 Nanoparticles

Dominique Piché,^{*,†,‡} Isabella Tavernaro,[‡] Jana Fleddermann,[‡] Juan G. Lozano,^{†,§} Aakash Varambhia,[†] Mahon L. Maguire,[¶] Marcus Koch,[‡] Tomofumi Ukai,[§] Armando J. Hernández Rodríguez,^{||} Lewys Jones,^{⊥,‡} Frank Dillon,[†] Israel Reyes Molina,^{||} Mai Mitzutani,^{†,ⓐ} Evelio R. González Dalmau,^{||} Toru Maekawa,[§] Peter D. Nellist,[†] Annette Kraegelh,[‡] and Nicole Grobert^{†,∇}

[†]Materials Department, University of Oxford, Parks Road, Oxford OX1 3PH, England

[‡]INM - Leibniz Institute for New Materials, Campus D2 2, 66123 Saarbrücken, Germany

[¶]British Heart Foundation Experimental Magnetic Resonance Unit, Wellcome Trust Centre for Human Genetics, Roosevelt Drive, Oxford OX3 7BN, England

[§]Bio-Nano Electronics Research Centre, Toyo University, 2100, Kujirai, Kawagoe, Saitama 350-8585, Japan

^{||}Departamento de Imágenes por Resonancia Magnética, Cuban Neurosciences Center, Street 190 e/25 and 27, Cubanacan Playa, Havana CP 11600, Cuba

[⊥]Advanced Microscopy Laboratory, Centre for Research on Adaptive Nanostructures and Nanodevices (CRANN), Dublin 2, Ireland

[#]School of Physics, Trinity College Dublin, Dublin 2, Ireland

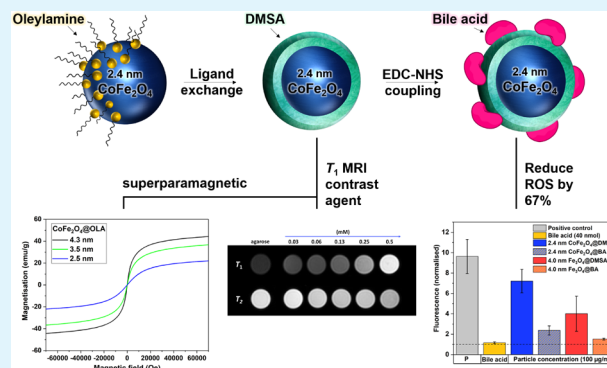
[ⓐ]Department of Material Science and Engineering, Tokyo Institute of Technology, S8-25, 2-12-1 Ookayama, Meguro-ku, Tokyo 152-8552, Japan

[∇]Williams Advanced Engineering, Grove, Oxfordshire, OX12 0DQ, England

Supporting Information

ABSTRACT: Extraordinarily small (2.4 nm) cobalt ferrite nanoparticles (ESCIoNs) were synthesized by a one-pot thermal decomposition approach to study their potential as magnetic resonance imaging (MRI) contrast agents. Fine size control was achieved using oleylamine alone, and annular dark-field scanning transmission electron microscopy revealed highly crystalline cubic spinel particles with atomic resolution. Ligand exchange with dimercaptosuccinic acid rendered the particles stable in physiological conditions with a hydrodynamic diameter of 12 nm. The particles displayed superparamagnetic properties and a low r_2/r_1 ratio suitable for a T_1 contrast agent. The particles were functionalized with bile acid, which improved biocompatibility by significant reduction of reactive oxygen species generation and is a first step toward liver-targeted T_1 MRI. Our study demonstrates the potential of ESCIoNs as T_1 MRI contrast agents.

KEYWORDS: cobalt ferrite nanoparticles, one-pot synthesis, magnetic resonance imaging, ligand exchange, cytotoxicity, ultrasmall nanoparticles, T_1 -weighted contrast agent, liver targeting



1. INTRODUCTION

Contrast agents (CA) are useful tools to enhance image contrast in magnetic resonance imaging (MRI). T_1 contrast agents, which shorten T_1 and generate positive (longitudinal) contrast, are primarily gadolinium (Gd)-based. With seven unpaired electrons, Gd provides effective T_1 relaxation of surrounding water protons by dipole interactions. As Gd ions are toxic, chelating agents are used to shield the body from exposure, which accelerate renal clearance and mitigate the toxicity. However, in a recent postmortem study by Mayo

Clinic researchers, Gd deposits were found in the brain tissue of patients who had received Gd contrast agent-enhanced MRI scans.¹ The potential for Gd dechelation raised fresh concerns over the safety of Gd-based agents, and in February 2018, the U.K. government suspended the licenses of Omniscan and

Received: October 3, 2018

Accepted: January 28, 2019

Published: January 28, 2019

Magnevist, two main commercial Gd-based contrast agents, until further investigation.²

The safety concerns for Gd-based agents prompted research into alternative materials, and recently, extremely small-sized iron oxide nanoparticles (<3 nm) emerged as a potential biocompatible approach.³ Larger superparamagnetic iron oxide nanoparticles (SPIONs) (>5 nm) have proven clinical utility for transverse (T_2) contrast enhancement through induction of local magnetic field inhomogeneities, which dephase nearby water protons, shortening both T_2^* and T_2 relaxation. As SPIONs are uptaken by the reticuloendothelial system and thus predominately accumulate in the liver,⁴ they proved suitable for liver-targeted MRI, and two types of SPIONs received FDA approval (Feridex and Resovist).⁵ However, Gd-based nonspecific and hepatospecific agents demonstrated better practicality and diagnostic performance for liver cancer and thus are currently preferred by clinicians.⁶ For liver MRI, T_1 -weighted contrast agents are beneficial for detecting metastases and liver lesions.⁷ Kim et al. recently showed that T_1 -weighted contrast could be achieved with iron oxide nanoparticles by reducing their size below 3 nm. In a size-dependent study with 1.5, 2.2, 3.0, and 12 nm maghemite particles,⁸ they found that the magnetic core of particles smaller than 3 nm was greatly reduced because they were composed mostly of surface atoms, which are magnetically disordered due to spin canting. This led to a decrease in T_2 effect, while the five unpaired electrons provided shortening of T_1 . Similar studies that echo this finding have since emerged.^{9–11}

Iron oxide offers a more biocompatible route than Gd because its degradation products can be stored by ferritin in the body. Although generally considered safe, there are toxicity concerns surrounding iron oxide and, particularly, other metal oxide nanoparticles such as cobalt ferrite, notably due to their potential to generate reactive oxygen species.¹² The toxicity of metal oxide nanoparticles, however, can be effectively mitigated through a biocompatible surface coating, and many different functionalization approaches have emerged.^{4,13} In addition to tailoring the surface of iron oxide nanoparticles, their magnetic properties can be customized by substituting ferrous ions with other metal ions. Substitution with cobalt ions introduces magnetic anisotropy, which has proved useful for biomedical applications such as magnetic hyperthermia,¹⁴ and Co^{2+} ions were recently shown to follow the same ferritin remediation pathway as iron.¹⁵ Cobalt ferrite (CoFe_2O_4) nanoparticles have also recently demonstrated high potential for MRI imaging with >5 nm particles, showing effective shortening of T_2 relaxation time.¹⁶ In comparison to magnetite, bulk CoFe_2O_4 possesses 90% saturation magnetization (M_s).¹⁷ The same was observed at the nanoscale, where 6 nm Fe_3O_4 and CoFe_2O_4 nanoparticles had M_s values of 55 and 50 emu g^{-1} , respectively.¹⁸ Considering that lower M_s values reduce T_2 effects and Co^{2+} cations have three unpaired electrons and Fe^{3+} has five, CoFe_2O_4 nanoparticles could be beneficial for T_1 -weighted MRI; however, to the best of our knowledge, it has not been explored before. In addition, CoFe_2O_4 is more resistant to oxidation,¹⁹ which can affect the magnetic properties,²⁰ as well as toxicity.¹² In this context, ESCIONs could be promising candidates for T_1 -weighted MRI applications.

Due to their large surface-to-volume ratio, the properties of particles <5 nm are sensitive to slight changes in their size, shape, and composition. Many existing methods have

demonstrated fine control over metal oxide particle size and shape at larger scales (>5 nm);^{21–24} however, control of these features below 5 nm remains a challenge and often requires the use of multiple solvents, surfactants, and reducing agents. Oleylamine, a long-chained alkylamine with a weak affinity for transition metals, can play a triple role of a solvent, surfactant, and reducing agent, mitigating the need for additional reagents. Nevertheless, to date, only a handful of studies have reported the synthesis of particles with oleylamine alone,^{25–27} and its role in controlling nanoparticle size is still not well understood.

Although synthesis by thermal decomposition offers superior size control in comparison to other methods such as coprecipitation, the particles produced are only dispersible in nonpolar solvents. One strategy to overcome this is to exchange the hydrophobic ligands for a hydrophilic ligand. Dimercaptosuccinic acid (DMSA), a small molecule composed of carboxylate and thiol groups, has a high affinity for transition metal ions and thus is effective at replacing ligands via a simple ligand exchange technique.²⁸ Additionally, DMSA is nontoxic and provides a chemically versatile surface for further functionalization.²⁹ Tailoring the surface of nanoparticles offers the potential for more specific therapeutic and diagnostic in vivo application, such as liver-targeted MRI. For liver-targeted applications, in addition to passive targeting by nanoparticle accumulation in the liver, active targeting with a hepatospecific functional group could be beneficial. Bile acids are amphipathic molecules with a hydrophilic chain and functional head group, which are uptaken into the liver via the hepatic pathway.³⁰ As such, they have been proposed as ideal surface modifiers for liver-targeted in vivo applications. Kramer et al. effectively demonstrated the use of bile acids as “Trojan horses” to deliver drugs specifically into the liver.³¹ Similarly, Zhang et al. found that functionalizing chitosan nanoparticles with cholic acid (CA), a primary bile acid, remarkably improved the efficacy of insulin delivery, owing to CA’s liver-targeting properties.³² Others have functionalized Gd chelates with CA toward liver-targeted MRI.^{33,34} To the best of our knowledge, bile acid-functionalized ferrite nanoparticles have not been explored before.

In this work, we report the synthesis, functionalization, and application of novel ESCIONs for T_1 -weighted MRI. A simple method for preparing ultrasmall MFe_2O_4 nanoparticles ($M = \text{Fe}, \text{Co}$) with subnanometer-size control is introduced. Following ligand exchange with DMSA, we obtained water-dispersible particles with small hydrodynamic diameters (~12 nm) that were stable in physiological conditions. As the same method and conditions were used to produce iron oxide and cobalt ferrite nanoparticles of the same size, we directly compare the effect of cobalt on the particles’ properties, as well as the induction of cytotoxic and oxidative stress effects to HepG2 cells. For the first time, ESCIONs are shown to act as T_1 MRI contrast agents. We further report the functionalization of ESCIONs with a bile acid derivative (cholic acid), which significantly reduced the production of reactive oxygen species (ROS) in labeled cells and is a promising step toward the development of safe liver-targeted MRI contrast agents.

2. EXPERIMENTAL SECTION

2.1. Synthesis of MFe_2O_4 ($M = \text{Fe}$ or Co) Nanoparticles. To synthesize CoFe_2O_4 nanoparticles, 0.02 mmol iron acetylacetonate ($\text{Fe}(\text{acac})_3$), 0.01 mmol cobalt acetylacetonate ($\text{Co}(\text{acac})_2$), and 60 mmol oleylamine (OLA) were placed into a three-neck flask fitted with a magnetic stirrer, reflux cooler, and thermometer. The mixture

was stirred at 400 rpm under argon for 10 min at room temperature before being heated to 225 °C at a heating rate of 14 °C min⁻¹. The solution was kept at this temperature for 10 min before allowing it to cool. The particles were then collected by centrifugation (4600 rpm, 10 min), washed in ethanol several times, and redispersed in cyclohexane. To prepare iron oxide nanoparticles, 0.03 mmol Fe(acac)₃ was used with the conditions described above. To remove excess oleylamine, the particles were dialyzed with SnakeSkin dialysis tubing (3.5 kDa molecular weight cut-off, 22 mm × 35 feet diameter, Thermo Scientific) in chloroform for 3 h, with the solvent exchanged at the 1.5 h mark.

2.2. Ligand Exchange with Dimercaptosuccinic Acid (DMSA). The ligand exchange method was adapted from a previously reported protocol.²⁹ MFe₂O₄@OLA particles were evaporated by rotary evaporation and redispersed in toluene at a concentration of 5 mg/mL. Five milliliters of the particle dispersion was added to a glass vial and sonicated for 5 min in an ultrasonic bath. A DMSA solution was prepared by mixing 200 mg of DMSA in 12 mL of dimethyl sulfoxide (DMSO) by sonication for 5 min. The DMSA solution was added to the nanoparticles and sonicated for 15 min and then stirred at room temperature for 48 h at 200 rpm. To terminate the reaction, 20 mL of ethanol was added, and the particles were magnetically separated. The supernatant was discarded, and the particles were washed three times in ethanol with centrifugation at 4600 rpm for 15 min. Following redispersion in water, the pH was adjusted to 10 using NaOH, and the particles were dialyzed in 500 mL of water (SnakeSkin dialysis tubing (3.5 kDa molecular weight cut-off, 22 mm × 35 feet diameter, Thermo Scientific)) for 24 h to remove excess DMSA. Finally, the pH was readjusted to 7 with NaOH, and the particles were filtered through a sterile 0.22 m membrane (Rotilab 668.1, Carl Roth GmbH).

2.3. Characterization. The particles were characterized with transmission electron microscopy (TEM) using a JEOL 3000F microscope (300 kV acceleration voltage) and annular dark-field scanning transmission electron microscopy (ADF-STEM) using an aberration-corrected JEOL ARM200F microscope operating at both 80 and 200 kV. Electron energy loss spectroscopy (EELS) was performed to analyze the elemental composition of the particles and the oxidation state of the metals. CrystalMaker was used to visualize the crystal structure. Particle diameters were measured from TEM images using automated nanomaterial measurement software developed in-house. Hydrodynamic diameter measurements were obtained using Nanotrak NPA 250 with an external probe. Samples were diluted to approximate concentrations of 30 μg/mL and irradiated with a HeNe laser (red light, 780 nm), and the intensity fluctuations of the scattered light (detected at a backscattering angle of 180°) were analyzed. Three independent measurement runs of 60 s were collected for each sample at a temperature of 20 °C. The mean hydrodynamic diameter was obtained using cumulant analysis and a size distribution using a regularization scheme by number. Zeta potential (ζ) measurements were performed using a Malvern Zetasizer Nano ZSP equipped with a 633 nm laser. Three independent measurements including several subruns of 10 s per subrun were performed for each sample at a temperature of 25 °C. The ζ potential was calculated from the nanoparticle electrophoretic mobility using Smoluchowski theory. Thermogravimetric analysis (TGA) was employed to determine the amount of ligand on the surface of the nanoparticles using PerkinElmer Pyris Diamond TG/DTA6300. Five milligrams of dried nanoparticles were heated to 900 °C at a heating rate of 10 °C min⁻¹ under nitrogen gas flowing at 80 mL/min. To verify ligand coating, Fourier transform IR spectroscopy (FTIR) was employed using Varian Excalibur FTS 3500 FTIR. Transmission electron microscopy investigations on DMSA- and bile acid-functionalized particles were performed using a JEOL JEM-2100 microscope with a LaB₆ cathode operating at an accelerating voltage of 200 kV. For cryogenic-TEM (Cryo-TEM) investigations, 3 μL of nanoparticle solution at a concentration of ~200 μg/mL was deposited onto a holey carbon TEM grid (type S147-4, Plano, Wetzlar, Germany) and then plunged into liquid ethane using a Gatan CP3 cryopluger. The frozen sample was transferred under liquid

nitrogen to a Gatan Cryo-TEM holder (model 914). TEM investigations were performed at 100 K using the same microscope conditions described above. To obtain elemental concentrations, inductively coupled plasma optical emission spectrometry (ICP-OES) measurements were conducted using Horiba Jobin Yvon Ultima 2 (pressure: 2.15 bar; flow: 0.75 L/min; Co: λ = 238.892 nm; Fe: λ = 238.204 nm). Samples were diluted 1:100 in H₂O. Subsequent calculations (section 9 in the Supporting Information) were performed to estimate the particle concentration. The magnetic properties of the particles in dried form were assessed using a superconducting quantum interference magnetometer (SQUID) (MPMS3, Quantum Design, Inc.).

2.4. Cell Culture. Adherent epithelial human hepatocarcinoma cells (HepG2) (German Collection of Microorganisms and Cell Cultures (DSMZ, Braunschweig, Germany)) were cultured in an incubator under humidified atmosphere at 37 °C with 5% CO₂ in Dulbecco's modified Eagle's medium (DMEM) supplemented with 10% (v/v) fetal bovine serum (FBS) (PAN-Biotech 3302-P291205) and dislodged using Cellstripper (Corning, Wiesbaden, Germany).

2.5. Cytotoxicity Analysis. To evaluate the toxicity of the nanoparticles toward HepG2 cells, CellTox Green assay was employed. Cells were dislodged using Cellstripper, counted by an automated cell counter (CASY Model TT, OLS-OMNI Life Science, Bremen, Germany), and seeded with a density of 75,000/mL (100 μL per well) in 96-well BRAND plates (plastic bottom, black walls). HepG2 cells were incubated with nanoparticles of different concentrations in RPMI-1640 medium supplemented with 10% FBS for 24 h at 37 °C. Cell death was measured by the CellTox Green assay (positive control is the lysis solution from the kit). Fluorescence measurements were obtained using a Tecan Infinite M200 Pro plate reader (excitation = 490 nm; emission = 525 nm). Fluorescence values were normalized to the negative control (cell medium = 1) and corrected for optical interference using the percentage interference values from Figure S13A,B (Supporting Information). Three independent assays were performed, and for each assay, samples were tested in triplicate. Particle-induced optical interference was assessed by repeating the protocol above in the absence of cells. To test for particle optical interference in the event of a positive result, 50 μL of 1% Triton X-100 was added per well and incubated with cells for 24 h at 37 °C, after which nanoparticles in RPMI-1640 medium supplemented with 10% FBS were added and fluorescence measurements were performed as above. Interference testing is detailed further in section 10 in the Supporting Information.

2.6. Reactive Oxygen Species Measurements. Nanoparticle-induced oxidative stress was measured by detecting the oxidation of 2',7'-dichlorofluorescein-diacetate (H₂DCF-DA) into the highly fluorescent compound 2',7' dichlorofluorescein (DCF) due to the presence of reactive oxygen species. Cells were dislodged using Cellstripper, counted by an automated cell counter (CASY Model TT, OLS-OMNI Life Science, Bremen, Germany), and seeded with a density of 75,000/mL (100 μL per well) in 96-well BRAND plates (plastic bottom, black walls). HepG2 cells were incubated with nanoparticles of different concentrations in RPMI-1640 medium supplemented with 10% FBS for 24 h at 37 °C. Hydrogen peroxide was used as the positive control. Following incubation, 100 μM H₂DCF-DA diluted in DMEM medium (without phenol red) was added to each well and incubated for 30 min at 37 °C. Fluorescence measurements were obtained using a Tecan Infinite M200 Pro plate reader (excitation = 492 nm; emission = 530 nm). Fluorescence values were normalized to the negative control (cell medium = 1) and corrected for optical interference using the percentage interference values from Figure S13A,B (Supporting Information). Three independent assays were performed, and for each assay, samples were tested in triplicate. Interference testing was conducted by incubating particles with H₂DCF in the absence of cells. H₂DCF-DA was deacetylated with NaOH according to the protocol of Ivask et al.³⁵ Nanoparticles or controls (water, PBS, or 10 μM 3-morpholinopyridone (SIN-1)) were incubated with 100 μL of H₂DCF for 1 h at 21 °C in the dark. Fluorescence measurements were then performed as above. To assess for particle reduction of the ROS

signal, an interference test was repeated as above with the addition of 10 μM SIN-1 per well.

2.7. 9.4 T Preclinical MRI Phantom Test. To evaluate the MRI contrast effect of ESCIOs, a phantom test was performed using a 9.4 T imaging system with 1 T/m imaging gradients and DirectDrive console (Agilent Technologies, USA), and a 39 mm i.d. quadrature-driven birdcage resonator was tuned to 400 MHz (Rapid Biomedical, Germany). Nanoparticles were linearly diluted in agarose gel (1% TBE blend) and suspended in 1 mL syringes. Following calibration and manual shimming, slice-selective gradient echo scout images were acquired (TR = 100 ms, TE = 1.33 ms, 20° flip angle, 32 averages, 128 × 128 points, 40 × 40 mm² field of view (FOV), 6 mm slice thickness). T_1 mapping was carried out using a slice-selective inversion recovery sequence with gradient echo imaging readout (TR = 20 s, TI = 0.02–19 s in 48 steps, 2 averages, 128 × 128 points, 40 × 40 mm² FOV, 6 mm slice thickness). T_2 mapping was carried out using a slice-selective spin-echo imaging sequence with multiple echos in readout (TR = 30 s, TE = 8 ms, 4 averages, 512 echos, 128 × 128 points, 40 × 40 mm FOV, 6 mm slice thickness). All MR data were processed and fitted using IDL8.2 (Harris Geospatial Solutions, USA). Images were zero-filled to a matrix size of 256 × 256 points and masked on the basis of the magnitude of the scout image before fitting. The mean and standard deviation for T_1 and T_2 of each phantom were calculated over a region of interest (ROI) placed in the center of each phantom. The r_1 and r_2 values were calculated from the slope of $1/T_{1/2}$ against particle concentration.

2.8. 3.0 T Clinical MRI Phantom Test. To obtain clinically relevant relaxivity values for ESCIOs, a phantom test was performed on a 3.0 T Siemens Prisma MRI scanner equipped with a 32-channel receive-only head coil. Nanoparticles were linearly diluted with agarose (1% TBE blend) and gelified in glass tubes. The glass tubes were then suspended in 1% agarose in a tank to enhance background signals and have a large enough volume for shimming. Following calibration, T_2 mapping was carried out by acquiring slice-selective turbo spin-echo images (TR = 2020 ms, TE = 8–397 ms in 24 steps, 3 averages, 150° flip angle, 320 × 320 points, 180 × 180 mm² FOV, 10 mm slice thickness). T_1 mapping was carried out using a slice-selective inversion recovery turbo spin-echo sequence (TR = 3 s, TI = 25–2500 ms in 9 steps, TE = 9.7 ms, 3 averages, 128 × 128 points, 129 × 180 mm² FOV, 6 mm slice thickness). All MR data were analyzed using custom MATLAB (MathWorks) routines. The mean and standard deviation for T_1 and T_2 of each phantom were calculated over a ROI placed in the center of each phantom. T_1 times were fitted using a MATLAB lsqcurve routine to the results of a Bloch simulation of the experimental parameters. T_2 times were fitted with an exponential decay curve. The r_1 and r_2 values were calculated from the slope of $1/T_{1/2}$ against particle concentration.

2.9. Synthesis of Amino Cholate. To conjugate bile acid derivatives to the nanoparticles, an amino group was required. Conversion of cholic acid (C1129-25g) to amino cholate was achieved by modifying the protocol of Zhou et al.³⁶ Cholic acid was converted to *N*-hydroxysuccinimide (NHS) ester using *N,N'*-dicyclohexylcarbodiimide (DCC) as the coupling reagent. The activated ester was transformed into cholate amide, which was reduced by lithium aluminium hydride solution (LiAlH₄) to afford amino cholate. A Schlenk line was used for all synthesis reactions, and solvents were extracted under argon. Cholic acid (535 mg), DCC (295 mg), and NHS (218 mg) were dissolved in anhydrous tetrahydrofuran (THF) (25 mL) and acetonitrile (2.5 mL). After 8 h at room temperature, the colorless solid formed was filtered out, and the filtrate was concentrated in vacuo to give a colorless foam (741 mg, 71% yield). A portion of this solid (370 mg) was dissolved in anhydrous dimethylformamide (DMF) (10 mL), and 30 mL of ammonia (25% ammonium hydroxide solution) was added. After 12 h at 50 °C, the precipitate was filtered and collected by suction filtration, washed with water (2 × 10 mL), and purified with column chromatography over silica gel (Silica 60 (0.063–0.2 mm, Macherey-Nagel GmbH & Co.)) using dichloromethane (DCM) and methanol (8:1 ratio) as the eluents to give a white powder (122 mg, 41% yield). The solid (100 mg) was dissolved in anhydrous THF (20 mL) under

N_2 . LiAlH₄ (15.2 mL in THF) was added slowly via a syringe. The reaction mixture was heated to reflux for 24 h. A small amount of ethyl acetate was added, and the solvent was concentrated in vacuo. Finally, the residue was purified with column chromatography over silica gel using DCM/methanol (10:1), pure methanol, and methanol/triethylamine (AB109928, ABCR GmbH) (50:1) as the eluents to give a colorless solid.

2.10. Conjugation of Amino Cholate to MF₂O₄@DMSA Nanoparticles. The DMSA-coated nanoparticles were conjugated to amino cholate via EDC-NHS coupling (1-ethyl-3-(3-dimethylamino-propyl)-carbodiimide, EDC). Eight milliliters of nanoparticles in H₂O (300 $\mu\text{g}/\text{mL}$) were added to a glass vial, and the pH was lowered to 5 using hydrochloric acid. EDC (22 μL) was added and stirred, then 100 mg of sulfo-NHS in 1 mL of H₂O was added, and the solution was stirred at room temperature for 20 min. Another 22 μL of EDC was added, and following 20 min of further stirring, 20 mg of amino cholate in 2 mL of H₂O and 20 μL of triethylamine was added dropwise to the NP solution, and the solution was stirred overnight. The NPs were collected via centrifugation (4600 rpm, 15 min) and washed in H₂O. Finally, the bile acid-functionalized NPs were dialyzed against H₂O for 2 h with one water change after 1 h and then filtered through a sterile filter membrane (5 μL pore size). Conjugation was qualitatively checked with a ninhydrin test using ninhydrin (72490-10g), ethanol, and acetic acid.

3. RESULTS AND DISCUSSION

3.1. Synthesis of Extraordinarily Small MF₂O₄ Nanoparticles. Extraordinarily small iron oxide (ESIOs) and cobalt ferrite nanoparticles (ESCIOs) were synthesized following thermal decomposition of iron and cobalt acetylacetonate precursors in oleylamine. Figure 1 shows

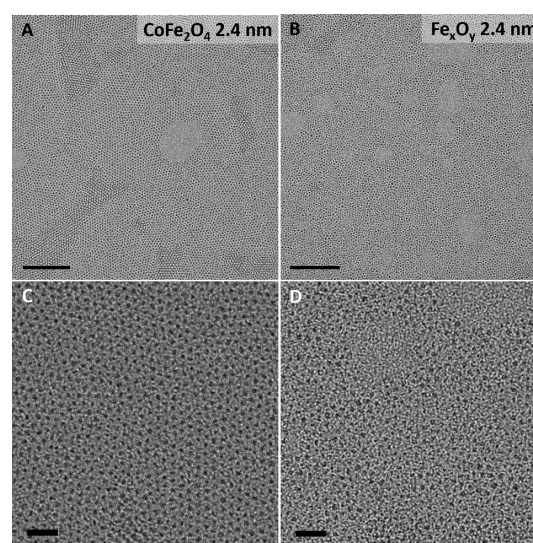


Figure 1. (A, B) TEM micrographs of 2.4 nm (A) ESCIOs and (B) ESIOs (scale bars are 100 nm). (C, D) Corresponding enlarged TEM micrographs of (C) ESCIOs and (D) ESIOs (scale bars are 20 nm).

monodisperse ESIOs and ESCIOs with sizes of 2.4 ± 0.4 nm under TEM. By varying the precursor-to-OLA ratio, particle size could be finely controlled from 2.4 to 4.6 nm. The same conditions were applied to synthesize both particle types; Table 1 compares the particle sizes measured for ESCIOs and ESIOs. The particles had a narrow size distribution (Figures S2 and S3), demonstrating the effectiveness of using oleylamine to control nanoparticle size in the ultrasmall regime. The threshold for size control by this method,

Table 1. ESIoN and ESCIoN Particle Size in Relation to Amount of Precursor when Synthesized with 60 mmol Oleylamine for 10 min at 225 °C^a

total amount of precursor (mmol)	TEM ESIoN size (nm)	TEM ESCIoN size (nm)
1.4	5.7 ± 3.0	4.3 ± 0.8
0.7	4.6 ± 0.6	4.0 ± 0.8
0.3	4.0 ± 0.4	3.5 ± 0.7
0.15	3.8 ± 0.5	3.3 ± 0.6
0.07	3.1 ± 0.5	3.0 ± 0.6
0.03	2.4 ± 0.4	2.4 ± 0.3

^aFor the synthesis of ESCIoNs, a ratio of 2:1 Fe/Co precursors was used throughout. Particle size decreases as the precursor(s)/oleylamine ratio decreases.

however, is a precursor/OLA molar ratio of 1:50, below which the size distribution was wide due to the formation of aggregates. Aggregate formation is likely due to an insufficient amount of surfactant present to cap the particles and restrict growth.

In addition to the relative amounts of reagents, heating rate, temperature, and reaction time are also known to affect particle size in thermal decomposition synthesis. We varied the heating rate from 12.6 to 24.7 °C min⁻¹ and found that this had no effect on particle size or shape (Figure S4). Similarly, raising the reaction temperature from 225 to 250 °C had no effect (Table S1). Extending the reaction time from 10 min to 1 h also led to no changes (Figure S5). Thus, the precursor/OLA ratio was the main influence on the particle size in our experiments. The decrease in particle size with the increase in oleylamine concentration could be attributed to oleylamine's role as a reducing agent, lowering the decomposition temperature and permitting nucleation to occur faster with an increasing precursor/OLA ratio.³⁷ An excess of oleylamine may also be required to ensure full coverage of the particles and prevent Ostwald ripening. Interestingly, changing the molar ratio of Fe/Co acetylacetonate precursors from 2:1 to 1.5:1 led to a wider size distribution for CoFe_xO_y particles (Figure S6), which may be due to the formation of two distinct crystalline phases.

ESIoNs and ESCIoNs were investigated with ADF-STEM to resolve their crystal structure. Particles synthesized with Fe(acac)₃ and oleylamine yielded a face-centered cubic (FCC) spinel structure (Figure 2A). Close inspection of the ADF-STEM image reveals a lattice fringe distance of 4.8 Å, which corresponds to the interplanar d-spacing of the (111) plane of magnetite/maghemite. ESCIoNs (2.4 nm) also had an FCC spinel structure (Figure 2B). ADF-STEM revealed a lattice fringe spacing of 2.4 Å, which is in good agreement with the interplanar d-spacing of the (311) plane of CoFe₂O₄. The Fourier transform was indexed to the [013] crystallographic orientation of CoFe₂O₄. To inspect the crystal structure in closer detail, multiframe fast acquisition and subsequent nonrigid alignment and averaging using SmartAlign³⁸ software were employed on a representative 4.3 nm CoFe₂O₄ particle. Figure 2C,D reveals an FCC spinel structure in the [110] zone axis orientation with atomic resolution and the corresponding crystal model. XRD patterns of 4.2 nm OLA-ESIoNs and 4.8 nm OLA-ESCIoNs also matched well with magnetite and cobalt ferrite cubic structures (JCPDS cards 01-075-0449 and 22-1086) (section 5 in the Supporting Information).

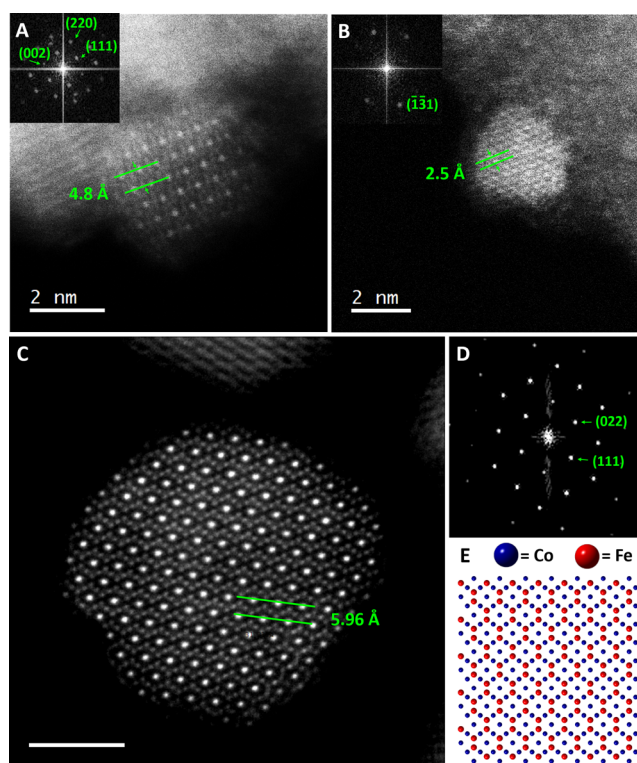


Figure 2. (A, B) ADF images and corresponding fast Fourier transform (FFT) of (A) 2.4 nm ESIoN in [110] zone axis orientation and (B) 2.4 nm ESCIoN in [013] zone axis orientation. (C, D) SmartAlign ADF image and corresponding FFT of a 4.3 nm ESCIoN in [110] zone axis orientation. Scale bar = 2 nm. (E) Modeled crystal structure of cobalt ferrite [110].

EEL spectroscopy detected the *K* ionization edge of oxygen and *L* ionization edge of iron, confirming that the ESIoNs are composed of iron and oxygen (Figure 3A). Quantification using the Hartree–Slater model showed an atomic ratio (*/O*) of 0.68 ± 0.07% for iron, which matches best with maghemite.^{39,40} Quantitative analysis of the Fe–*L*_{2,3} ionization edges can also indicate the oxidation state of iron oxide because the (*L*₃/*L*₂) intensity ratio varies depending on the oxidation state.⁴¹ The intensity ratio of *L*₃/*L*₂ was found to be 4.49, which is in good agreement with the value for magnetite.⁴¹ To further investigate the oxidation state, we examined the shape of the Fe 2p *L*₃ edge, which differs depending on the oxidation state, with magnetite presenting a shapeless *L*₃ peak and maghemite displaying a pre-shoulder.⁴² The inset of Figure 3A shows the *L*₃ peak in closer detail; the *L*₃ edge is smooth without a shoulder, which also suggests that the composition of the particles is Fe₃O₄. Due to their small size, it is possible that the particles are a mixture of magnetite and maghemite or that they oxidize to maghemite over time. Differentiating between the two is notoriously challenging at the nanoscale, and it was not possible to quantitatively distinguish between them. Nonetheless, the black color of the ESIoNs (Figure S1) strongly suggests that the particles are predominantly magnetite.⁴³ EEL spectroscopy of 2.4 nm ESCIoNs revealed three peaks corresponding to the *K* ionization edge of oxygen and *L* ionization edges of iron and cobalt, confirming the presence of cobalt in the particles (Figure 3B). Quantitative analysis of the EELS spectrum using the Hartree–Slater model revealed a relative composition of 56 ± 6% oxygen, 27 ± 3% iron, and 17 ± 2% cobalt, which

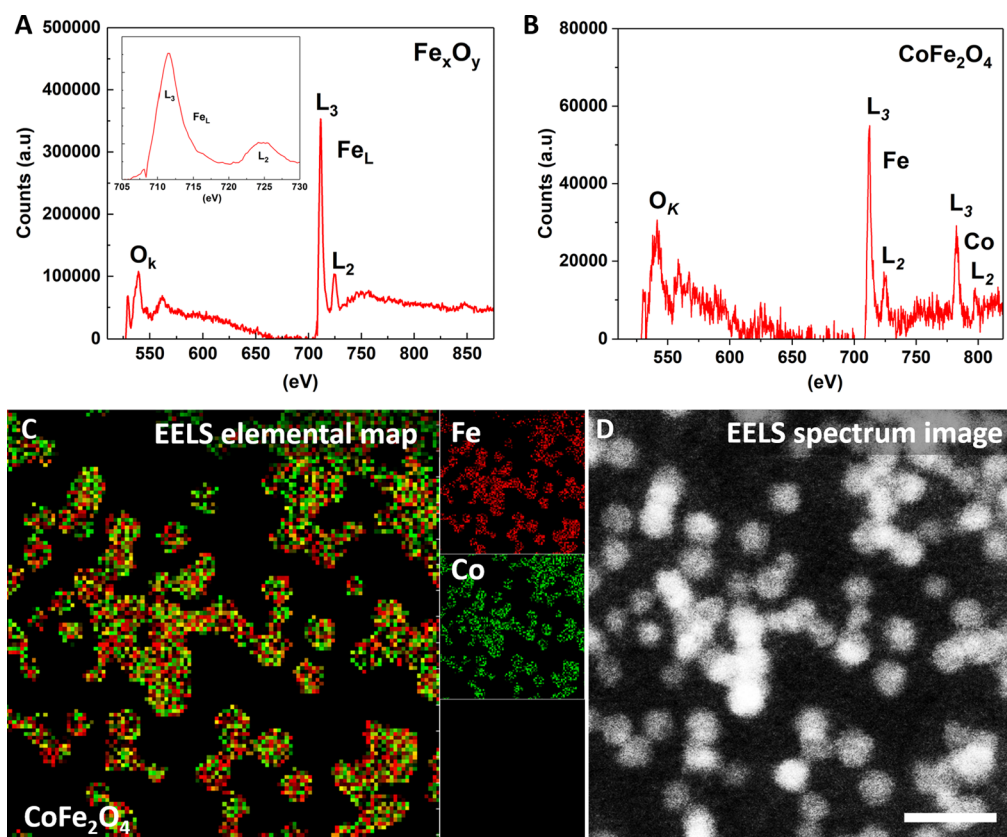


Figure 3. (A) EELS spectrum of ESIoNs showing the oxygen *K* and iron *L* ionization edges and (inset) *L* edges in the range of 705–730 eV presenting a smooth *L*₃ peak. (B) EELS spectrum of 2.4 nm ESCIoNs showing three peaks corresponding to the oxygen *K* and iron and cobalt *L* ionization edges. (C) EELS elemental map (red = iron, green = cobalt) showing a homogeneous distribution of cobalt and iron atoms in 3 nm ESCIoNs. (D) Corresponding EELS spectrum image (scale bar = 10 nm).

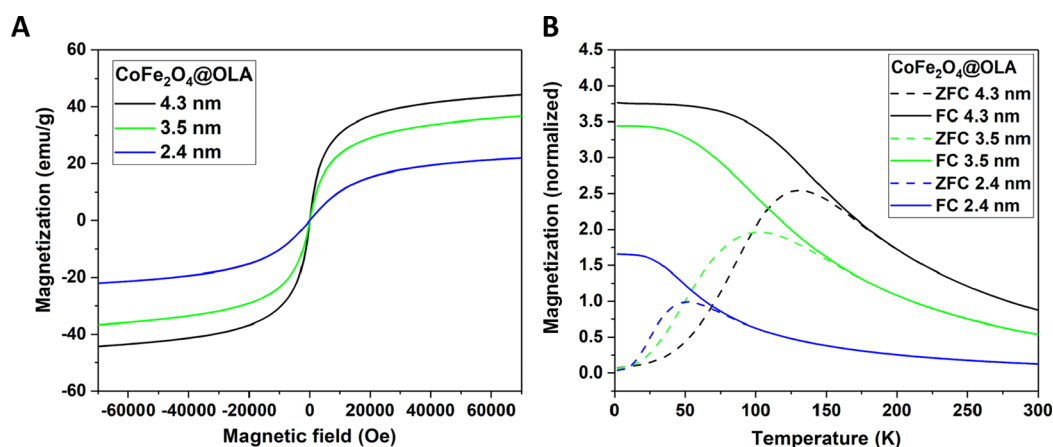


Figure 4. (A) Magnetization curves of 4.3, 3.5, and 2.4 nm OLA-ESCIoNs at 300 K. (B) Corresponding temperature-dependent magnetization (zero-field cooling (ZFC) and field-cooling (FC)) curves. The FC curves were obtained at an applied field of 100 Oe.

corresponds well with the composition of cobalt ferrite (CoFe_2O_4). EELS elemental mapping revealed a homogeneous distribution of cobalt and iron in the particles (Figure 3C).

The magnetic properties of 4.3, 3.5, and 2.4 nm OLA-ESCIoNs were assessed. The particles displayed typical superparamagnetic behavior with a loss of hysteresis (Figure 4A). The magnetization saturation (M_s) decreased with particle size, as anticipated, with 4.3, 3.5, and 2.4 nm particles having M_s values of 44, 37, and 22 emu/g, respectively, at 300 K. Analogously, the blocking temperature (T_B) decreased with particle size from 131 to 101 and 52 K for 4.3, 3.5, and 2.4 nm

particles (Figure 4B). The magnetic properties were reassessed following ligand exchange with DMSA, as detailed in the next section.

3.2. Ligand Exchange with DMSA: Colloidal Stability.

DMSA ligand exchange is a well-established method for transferring metal oxide nanoparticles from nonpolar solvents to water.²⁸ Oleylamine-coated particles were initially hydrophobic, owing to the hydrocarbon tail of OLA molecules. Following ligand exchange with DMSA, water-dispersible DMSA-ESIoNs and DMSA-ESCIoNs were obtained. The suspensions appeared clear, and no precipitation was visible,

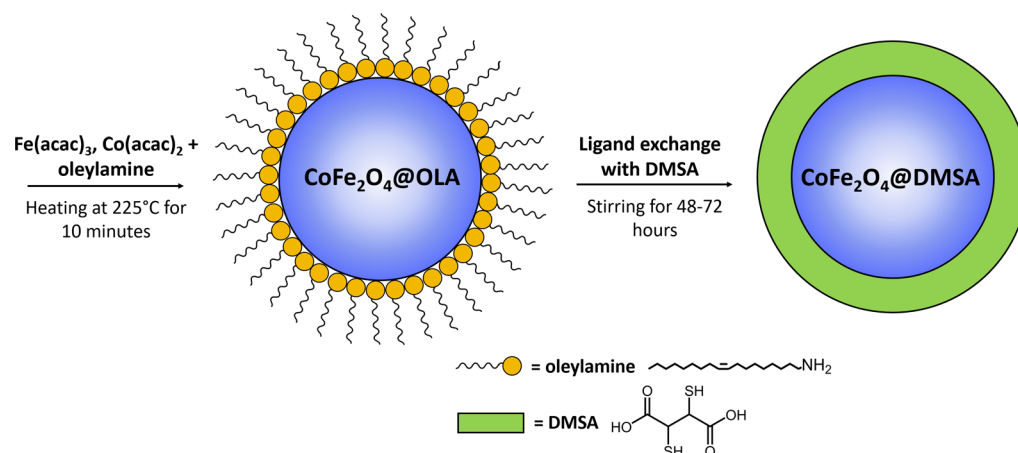


Figure 5. Oleylamine-coated ESCIoNs and ESIoNs are obtained following synthesis with acetylacetonate precursors and oleylamine at 225 °C for 10 min. Initially hydrophobic, the particles are rendered hydrophilic by stirring with DMSA for 48–72 h. DMSA preferably binds to the metal oxide core, replacing the oleylamine ligands.

Table 2. Details of Ligand Exchange Results with ESCIoNs and ESIoNs^a

sample	core size (nm)	D_h (nm)	zeta (ζ) (pH 7)	pH stability range ($\zeta \geq -25$ mV)	D_h (+ no. of months after measurement)
ESCIoN1	2.4 ± 0.4	11 ± 2	-31.8 ± 1.8	3–9	25 ± 7 (+12)
ESCIoN2	2.4 ± 0.4	13 ± 3	-34.2 ± 1.4	3–9	46 ± 14 (+3)
ESCIoN3	2.3 ± 0.3	16 ± 4	-28.0 ± 0.3	3–9	15 ± 5 (+3)
ESCIoN4	2.3 ± 0.3	8 ± 2	-42.2 ± 3.7	3–9	46 ± 16 (+12)
ESCIoN5	4.3 ± 0.6	12 ± 3	-38.4 ± 0.9	3–9	36 ± 7 (+12)
ESCIoN6	4.3 ± 0.6	23 ± 7	-40.7 ± 0.6	3–9	22 ± 4 (+12)
ESIoN1	2.4 ± 0.5	7 ± 2	-33.9 ± 0.7	5–9	40 ± 10 (+12)
ESIoN2	4.0 ± 0.8	12 ± 2	-43.5 ± 2.5	5–9	23 ± 6 (+3)
ESIoN3	4.2 ± 0.7	12 ± 2	-41.7 ± 1.0	5–9	24 ± 5 (+12)
ESIoN4	4.7 ± 0.7	16 ± 4	-43.2 ± 6.5	5–9	16 ± 3 (+12)

^aThe hydrodynamic diameters were measured using dynamic light scattering and repeated 3–12 months later. The pH stability range was determined by zeta potential values that exceeded -25 mV. ESCIoNs were stable in a pH range of 3–10, whereas ESIoNs were stable in solutions from pH 5 to 10. The DMSA ligand exchange method was reproducible for both particle types, and only minor flocculation had occurred in some samples after 12 months.

indicating that DMSA had bound to the nanoparticles. A summary of the synthesis and ligand exchange process is outlined in Figure 5. Hydrodynamic diameters (D_h) of 11 ± 2 and 8 ± 2 nm were measured for ESCIoN and ESIoNs, respectively. Their zeta (ζ) potentials were -31.8 ± 1.8 and -33.9 ± 0.7 mV, reflecting the negative charges from carboxylate moieties on the surface.

The stability of particles is critical for MRI because particle aggregation has a significant effect on relaxation rate. Aggregation of ultrasmall iron oxide nanoparticles has been shown to decrease the T_1 relaxation rate and increase the T_2 relaxation rate of nearby water protons, resulting in a dominant T_2 effect.⁴⁴ Cell toxicity is also affected by particle stability because aggregation can influence uptake into cells, and particle degradation due to acidic pH can lead to leaching of ions.⁴⁵ To address the stability and reproducibility, we performed DMSA ligand exchange with a range of ESCIoNs and ESIoNs with sizes of 2–5 nm and measured their D_h 's and ζ potentials in solutions from pH 3–10. Hydrodynamic diameters were remeasured following 3–12 months storage at 4 °C. D_h 's ranged from 7 to 23 nm and ζ potentials ranged from -28.0 to -43.2 mV, indicating that monodisperse and stable dispersions were initially obtained for all samples (Table 2). Following storage for 3–12 months, D_h 's increased slightly; the largest increase was from 8 to 46 nm after 12 months.

Interestingly, DMSA-ESCIoNs were found to be stable in a wider pH range of 3–10 than DMSA-ESIoNs, which began to flocculate below pH 5. As shown in Figure 6A, the D_h of DMSA-ESCIoNs increases slightly from 8 ± 2 nm at pH 7 to 17 ± 4 nm at pH 3, whereas the D_h of DMSA-ESIoNs increases from 7 ± 2 to 79 ± 25 nm. DMSA-ESIoN flocculation may be caused by acid-induced reduction of Fe³⁺ to Fe²⁺, which in turn causes oxidation of DMSA. Alternatively, DMSA may have oxidized from oxygen in the solution. Oxidation of DMSA is a known phenomenon that leads to the formation of interparticle disulfide bridges. Fauconnier et al.²⁸ found that addition of an alkalization step after ligand exchange improved colloidal stability significantly. At pH 9, the free SH groups are deprotonated to thiolate groups, which partially replace carboxylate groups at the surface of the particles. Free COO⁻ groups then serve to stabilize the particle in a wide pH range. Our observations concur with that of Fauconnier; visible sedimentation of the particles occurred in the absence of an alkalization step. Similar remarks were made by Chen et al.⁴⁶ who observed sedimentation of DMSA-coated nanoparticles within five days. In alkaline conditions, conversion of S–H groups to thiolate groups is promoted by DMSA and pH-induced oxidation of Fe³⁺ to Fe²⁺,²⁸ resulting in fewer S–H groups on the surface. As cobalt ferrite is more resistant to oxidation than

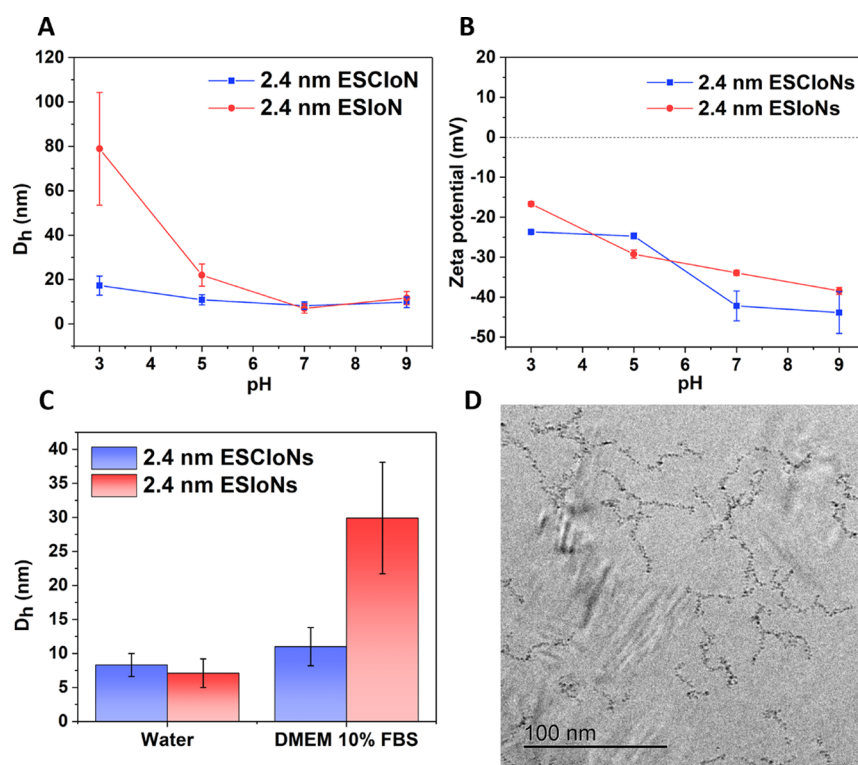


Figure 6. (A) Hydrodynamic diameters and (B) zeta potentials of 2.4 nm DMSA-ESCIoNs and DMSA-ESIoNs in pH range 3–9. (C) Comparison of their D_h 's in water and cell medium. (D) Cryo-EM micrograph of ESCIoNs in water.

magnetite, more S–H groups may be left free on the surface to stabilize the particles in acidic pH. In addition to an alkalization step, we found that dialyzing particles to remove excess oleylamine prior to ligand exchange helped to reproducibly obtain small hydrodynamic diameters. Without prior dialysis, larger D_h 's were obtained (116 ± 54 vs 17 ± 3 nm for dialyzed particles) (Figure S10).

To view the particles in their native liquid state, cryo-EM was employed. Figure 6D shows DMSA-ESCIoNs arranged in a chain-like fashion, possibly due to magnetic interactions. Higher particle concentrations were used for cryo-EM than for hydrodynamic diameter measurements, owing to the difficulty in locating such small-sized nanoparticles in a suitably thin area of ice for optimum imaging. Magnetic nanoparticles in high concentration are known to have weak magnetic dipole interactions, resulting in linear chains.⁴⁷ When dilute samples were used for cryo-EM, the micrographs revealed monodisperse nanoparticles (Figure S11A). The particles retained their original core size post exchange, whereas Ostwald ripening or particle dissolution has been reported by others.^{29,48} The stability of particles in water is important for their general application and storage; however, in vivo, the particles will encounter more complex media containing proteins, lipids, salts, and other large molecules, which may interact with the particle. The formation of a protein–particle complex, named the protein corona, can potentially alter the surface charge and hydrodynamic diameter of the particles, affecting their in vivo distribution.⁴⁹ As a first step to assess protein adsorption onto DMSA particles, we measured the D_h of the particles in cell culture medium DMEM supplemented with 10% FBS. Figure 6C shows no significant change in D_h for ESCIoNs (8 ± 2 nm in pure water to 11 ± 3 nm in DMEM with 10% FBS), suggesting that protein adsorption was

minimal. ESIoNs suffered a larger increase from 7 ± 2 to 30 ± 8 nm, indicating protein adsorption. Cryo-EM of DMSA-ESIoNs in DMEM revealed no additional agglomeration or aggregation in comparison to DMSA-ESIoNs in water, suggesting that the increase in D_h was due to protein adsorption (Figure S11B).

To confirm DMSA binding to the particles, TGA and FTIR studies were conducted. Figure 7 shows the weight loss profiles

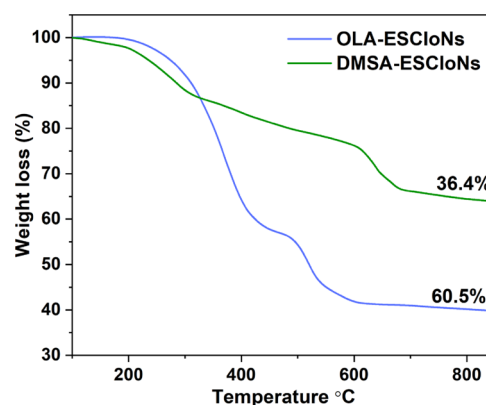


Figure 7. TGA weight loss profile of 2.4 nm OLA-ESCIoNs and DMSA-ESCIoNs.

of OLA-ESCIoN and DMSA-ESCIoN particles with a total weight loss of 60.5 and 36.4%, respectively. The amount of ligands present on the surface of the nanoparticles was estimated from the weight loss using eq 1 below

$$N = \frac{\omega_p \rho \nu A}{\omega_c M} \quad (1)$$

where ω_1 is the total weight (in grams) of the ligands calculated from TGA, ρ is the density of cobalt ferrite (5.2957 g/cm^3), ν is the volume of the 2.4 nm particle, A is the Avogadro's constant, ω_c is the total weight (in grams) of the particle core (calculated from TGA), M is the molar mass of the ligand (oleylamine (267.5 g/mol) or DMSA (182.22 g/mol)), and N is the number of ligands per particle. The estimated number of DMSA ligands per particle is 90. Considering the surface area of a 2.4 nm particle is 18.1 nm^2 , the ligand density is approximately 5 molecules/ nm^2 . Therefore, the weight loss of 36.4% suggests that a double layer of DMSA is present on the particle's surface. The amount of oleylamine totaled 98 molecules per particle; thus, the ligand density for a 2.4 nm particle is approximately 5.4 molecules/ nm^2 , suggesting that a small amount of excess oleylamine was present after dialysis.

FTIR of OLA-ESCIoNs and DMSA-ESCIoNs showed clear differences in their spectra (Figure 8). The first peak at 550

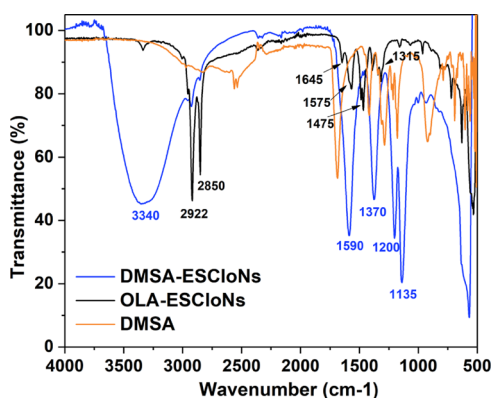


Figure 8. FTIR spectra of 2.4 nm OLA-ESCIoNs, DMSA-ESCIoNs, and DMSA. Sharpening and separation of the peaks at 1590 and 1370 cm^{-1} in the DMSA-ESCIoN particles spectrum are due to asymmetric and symmetric stretching of carbonyl groups, respectively, indicating that DMSA is bound to the surface.

cm^{-1} is typical of the Fe–O stretching mode. An intensity reduction of this peak was observed following ligand exchange, which shows that DMSA has irreversibly adsorbed to the surface of the particles.⁵⁰ Broad peaks at 2922 and 2850 cm^{-1} are attributed to CH_2 asymmetric and symmetric stretching, respectively. The set of broad peaks between 1300 and 1650 cm^{-1} in OLA-ESCIoNs are due to $-\text{NH}_2$ bending modes. The

strong broad band at 3340 cm^{-1} is due to $-\text{OH}$ stretching. The presence of this band and the peak at 1135 cm^{-1} after ligand exchange is due to OH groups from remnant water. Sharpening and separation of the peaks at 1590 and 1370 cm^{-1} appear from asymmetric and symmetric stretching of carbonyl groups, respectively, indicating that DMSA is bound to the surface.⁵⁰ These new peaks were assigned to red shifting of carbonyl absorption bands typically observed at 1700 and 1750 cm^{-1} . Shifting occurred because the ligand is bound to the particles, resulting in disassociation of the carboxyl group. Large splitting between these bands is associated with a monodentate interaction between the carboxylate group of DMSA and the iron oxide nanoparticle.²⁹

The magnetic properties of 2.4 nm DMSA-ESCIoNs and DMSA-ESIoNs were measured after ligand exchange with DMSA, as the surface ligand is known to influence their magnetic behavior.⁵¹ Indeed, we found that, following ligand exchange of OLA for DMSA, the M_s and T_B of ESCIoNs and ESIoNs decreased (Figure S12). Figure 9 shows the magnetization curves at 300 K, with both DMSA-ESCIoNs and DMSA-ESIoNs displaying typical superparamagnetic behavior evidenced by a loss of hysteresis. The magnetization saturation of 2.4 nm DMSA-ESIoNs and DMSA-ESCIoNs was 9.6 and 4.8 emu/g , respectively. The blocking temperature (T_B) for 2.4 nm DMSA-ESCIoNs was 102 K, which is markedly higher than that of DMSA-ESIoNs at 12 K (Figure 9B). This rise in T_B is characteristic for CoFe_2O_4 due to an increase in anisotropy energy courtesy of Co^{2+} ions. Their magnetic moments (m) calculated from eq 2 were 38.8 B for DMSA-ESIoNs and $17.5 \mu\text{B}$ for DMSA-ESCIoNs

$$m = \frac{M\rho V}{\mu_B} \quad (2)$$

where M is the mass magnetization, ρ is the material density, V is the particle volume, and μ_B is the Bohr magneton value.⁸ The very small magnetic moment of 2.4 nm particles results from a high proportion of the particle being composed of surface atoms and thus subject to spin canting effects.⁵²

3.3. Cytotoxicity and Oxidative Stress of ESCIoNs and ESIoNs. For biomedical applications, it is paramount that nanoparticles are screened for potential cytotoxic effects. The cytotoxicity of DMSA-ESIoNs and DMSA-ESCIoNs toward HepG2 cells was evaluated. HepG2 cells were chosen for the cytotoxicity study because metal oxide particles that are not renally cleared typically accumulate in the liver following in

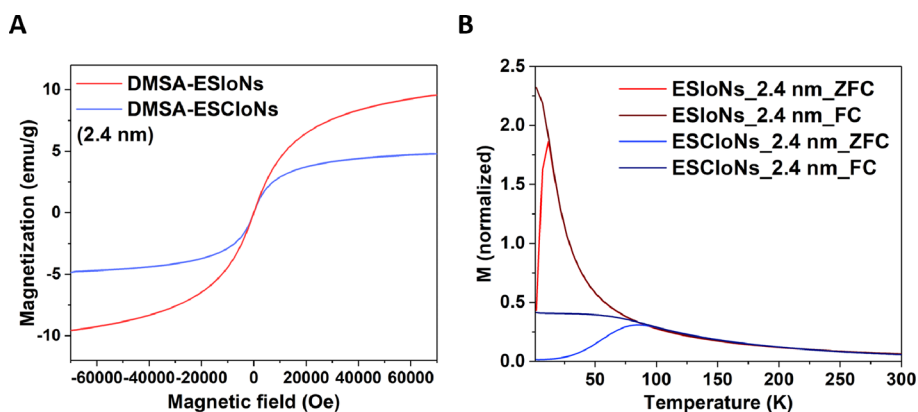


Figure 9. (A) Magnetization curves of 2.4 DMSA-ESIoNs and DMSA-ESCIoNs at 300 K. (B) Corresponding temperature-dependent magnetization (zero-field cooling (ZFC) and field-cooling (FC)) curves. The FC curves were obtained at an applied field of 100 Oe.

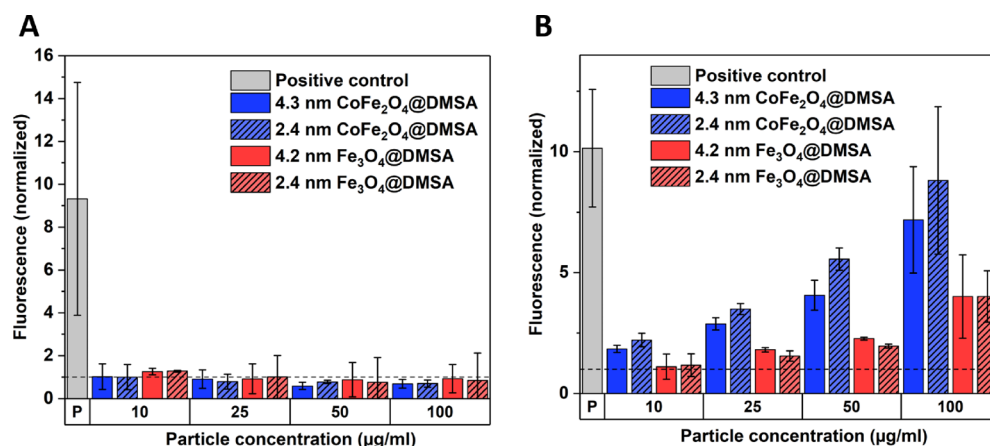


Figure 10. Comparison of cytotoxicity and oxidative stress measurements of DMSA-ESiONs and DMSA-ESCIoNs toward HepG2 cells. Values were normalized to the negative control (cell medium = 1). (A) Relative cell death (fluorescence) in relation to particle concentration. No cell death was observed for any particle type. The positive control is the lysis solution from the kit. (B) Relative ROS production (fluorescence) induced by the particles. Both DMSA-ESiONs and DMSA-ESCIoNs produced ROS; however, DMSA-ESCIoNs produced significantly higher amounts than DMSA-ESiONs. The positive control is hydrogen peroxide. Results are shown as mean \pm standard deviation from three independent experiments.

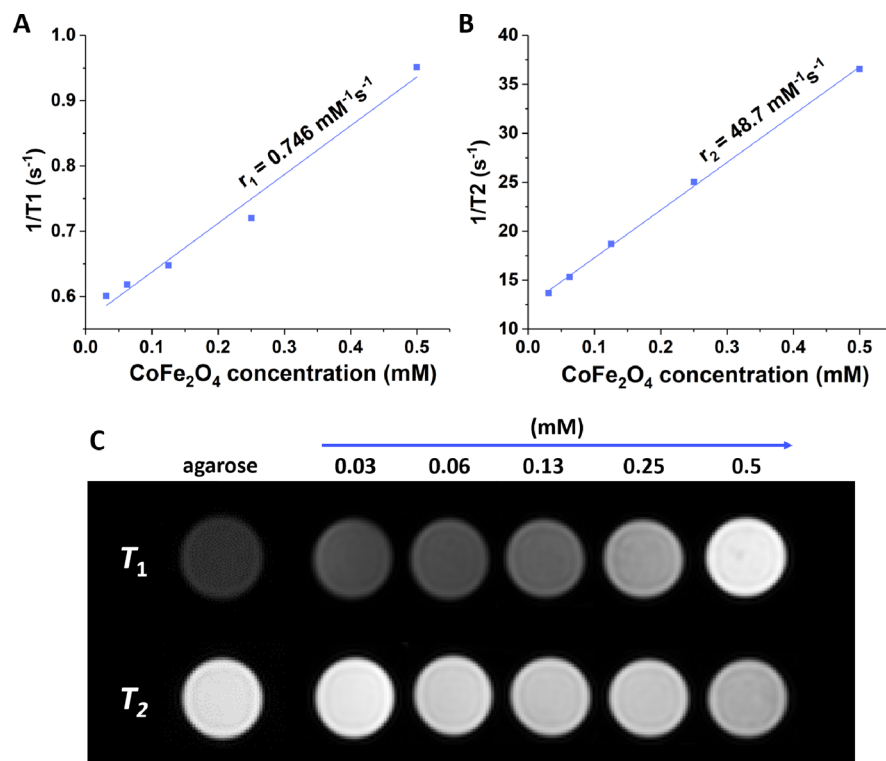


Figure 11. 9.4 T MRI phantom test of 2.4 nm DMSA-ESCIoNs embedded in 1% agarose gel. (A) Plot of r_1 relaxation rate and (B) r_2 relaxation rate against DMSA-ESCIoN particle concentration. (C) MRI scout image showing the increase in T_1 (positive) contrast with increasing particle concentration. The particles have a less pronounced effect on the T_2 (negative) contrast, decreasing slightly with increasing concentration.

vivo distribution,¹⁵ and the intended design of the particles is toward liver-targeted MRI contrast enhancement. Figure 10A shows relative cell death for DMSA-ESCIoNs and DMSA-ESiONs at concentrations up to 100 $\mu\text{g/mL}$. Relative cell death (fluorescence) was corrected for optical interference induced by the particles (see section 10 in the Supporting Information). No cell death occurred with any particle types, and there was no size or metal composition influence.

In tandem with cytotoxicity testing, we evaluated nanoparticle-induced production of reactive oxygen species using

2',7'-dichlorofluorescein-diacetate (H₂DCF-DA). Reactive oxygen species have potentially harmful effects on cells and have been linked to DNA damage, apoptosis, and even carcinogenesis.⁵³ Conversely, nanoparticle-induced ROS production can be harnessed for therapeutic application as a treatment toward cancer cells through selective induction of apoptosis.⁵⁴ In our measurements, both DMSA-ESiONs and DMSA-ESCIoNs produced ROS in contact with HepG2 cells. DMSA-ESCIoNs produced much higher amounts of ROS in comparison to DMSA-ESiONs at particle concentrations of

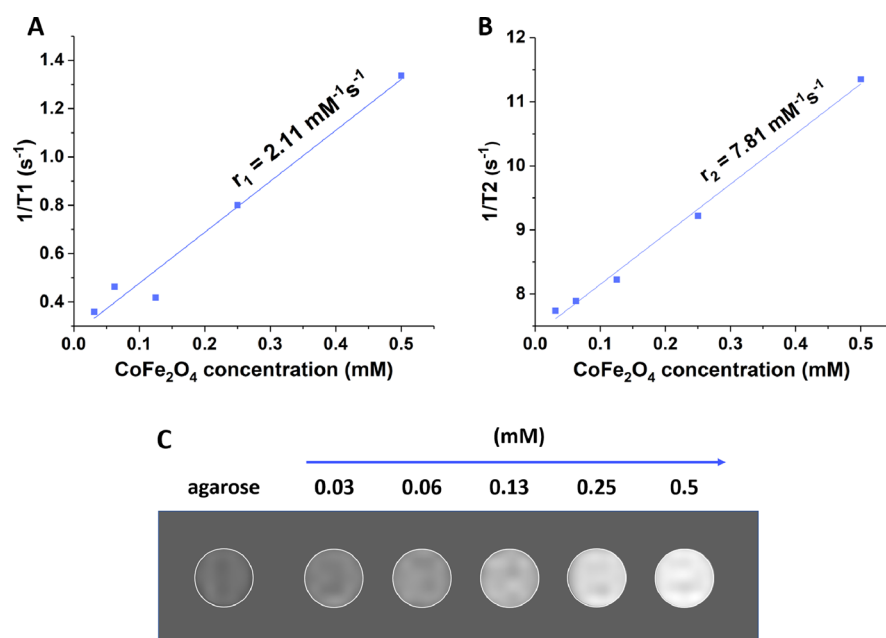


Figure 12. 3.0 T MRI phantom test of 2.4 nm DMSA-ESCIoNs embedded in 1% agarose gel. (A) Plot of r_1 relaxation rate and (B) r_2 relaxation rate against DMSA-ESCIoN particle concentration. (C) MRI scout image showing the increase in T_1 (positive) contrast with increasing particle concentration.

Table 3. Comparison of Relaxation Properties of Other Ultrasmall Ferrite Nanoparticle Systems and Commercially Available Contrast Agents at 3.0 and 9.4 T^a

nanoparticle/coating	D_{TEM} (nm)	D_{h} (nm)	r_1 ($\text{mM}^{-1} \text{s}^{-1}$)	r_2 ($\text{mM}^{-1} \text{s}^{-1}$)	r_2/r_1	B_0 (T)	reference
CoFe ₂ O ₄ @DMSA	2.4	11	2.11	7.81	3.70	3.0	this work
Fe ₂ O ₃ @PO-PEG (ESIoNs)	2.2	15	4.77	17.5	3.67	3.0	8
MnFe ₂ O ₄ /mPEG	2.0	8	8.43	21.02	2.49	3.0	11
Magnevist (Gd-DTPA)	n/a	n/a	3.7	5.2	1.41	3.0	61
Gadovist (Gd-DO3A-butrol)	n/a	n/a	5.0	-7.1	1.42	3.0	61
CoFe ₂ O ₄ @DMSA	2.4	11	0.75	48.7	65	9.4	this work
γ -Fe ₂ O ₃ /citrate	2.0	4	0.25	12.4	49.6	9.4	62
Resovist	5	63	1.67	374.6	224.3	9.4	63

^an/a: not available.

100 g/mL. Metal oxide-induced production of ROS is linked to the Fenton reaction,⁵⁵ whereby transition metal ions catalyze hydrogen peroxide decomposition with generation of hydroxyl radicals.⁵⁶ The increase in ROS production for DMSA-ESCIoNs may be due to the higher catalytic ability of Co²⁺ ions over Fe²⁺.⁵⁶ It may also be linked to the production of different ROS species; iron is known to produce $\cdot\text{OH}$ radicals, whereas cobalt produces $\cdot\text{HO}_2$ radicals.⁵⁷ Other studies have reported ROS production by Fe₃O₄ and CoFe₂O₄ nanoparticles.⁵⁴ Conversely, others have reported no cytotoxic effects or ROS production for CoFe₂O₄ nanoparticles against HepG2 cells.⁵⁸ This disparity highlights the importance of testing each new particle system against cells, as surface coating, preparation parameters, and other slight changes in particle characteristics can have an effect. Frequently, metal oxide nanoparticles are tested only for cytotoxic effects and not for oxidative stress, despite their known capability for producing ROS. In section 3.5 of this paper, we demonstrate a route to minimize ROS production via functionalization with a bile acid derivative.

3.4. MRI Phantom Tests of 2.4 nm DMSA-ESCIoNs.

Iron oxide nanoparticles have been extensively explored for MRI contrast enhancement applications; however, despite

promise in other biomedical applications such as magnetic hyperthermia and drug delivery, cobalt ferrite particles remain relatively unexplored as MRI contrast agents. A few reports exist detailing the potential of cobalt ferrite nanoparticles >3 nm as T_2 contrast agents, owing to their large magnetic moment. Ghasemian et al.⁵⁹ measured the relaxivity of DMSA-coated 16 nm cobalt–zinc ferrite nanoparticles and found their suitability for T_2 contrast enhancement with an r_2/r_1 ratio of 50 (measured at 1.5 T). Nidhin et al.⁶⁰ reported an r_2/r_1 ratio of 6.9 for 7.2 nm cobalt ferrite nanoparticles. However, cobalt ferrite nanoparticles smaller than 3 nm have not been tested for MRI applications before.

To assess the potential of 2.4 nm DMSA-ESCIoNs as MRI contrast agents, we designed a phantom test using linearly decreasing particle concentrations and a 9.4 T MRI scanner. Figure 11 shows T_1 and T_2 phantom images of DMSA-ESCIoNs embedded in 1% agarose and the corresponding relaxation curves. T_1 (positive) contrast increases with increasing concentration, whereas little influence on T_2 (negative) contrast was observed (Figure 11C). The r_1 relaxivity, calculated from the slope of T_1 relaxation time against particle concentration, was $0.75 \text{ mM}^{-1} \text{ s}^{-1}$. The r_2 relaxivity, calculated from the slope of T_2 relaxation time

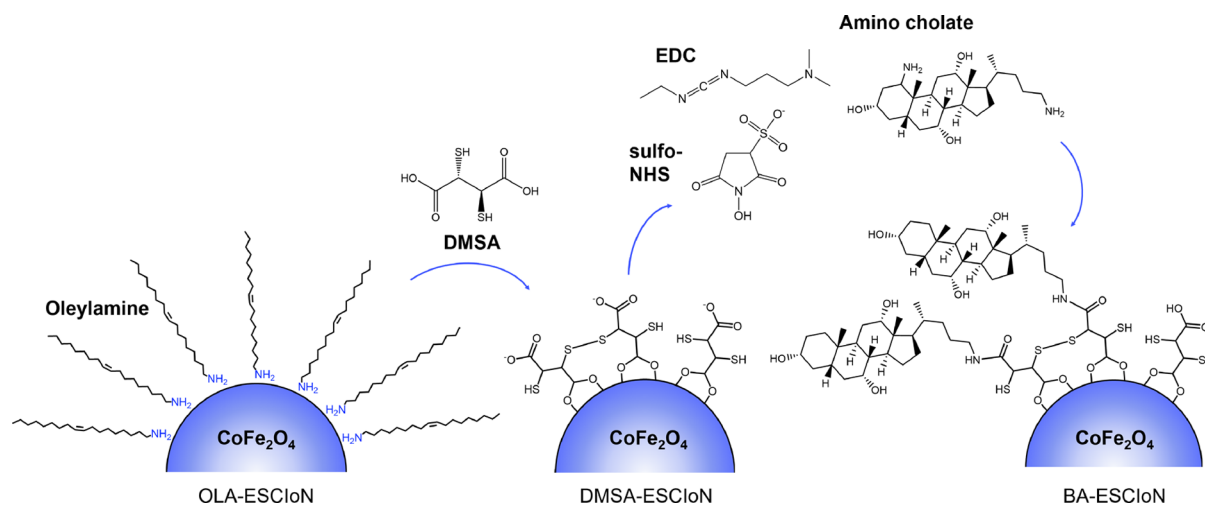


Figure 13. Schematic outlining the synthesis process for BA-ESCIoNs and BA-ESIoNs. First, hydrophobic oleylamine-coated particles are rendered hydrophilic via DMSA ligand exchange. Then, DMSA-coated nanoparticles are conjugated to amino cholate by EDC-NHS coupling.

against particle concentration, was $48.7 \text{ mM}^{-1} \text{ s}^{-1}$. The r_2/r_1 ratio is an important parameter for determining the effectiveness of a contrast agent toward r_1 or r_2 relaxation: the higher the r_2/r_1 ratio, the more effective the agent is toward T_2 contrast. The r_2/r_1 ratio we obtained for DMSA-ESCIoN nanoparticles at 9.4 T was 65. The high ratio is due to the large magnetic field strength of the system used because the r_2/r_1 ratio increases with the increase in magnetic field strength (r_1 decreases and the r_2 increases).⁶¹ Following initial testing at 9.4 T, we conducted a further MRI phantom test using a 3.0 T clinical MRI system. The phantom setup consisted of nanoparticle–agarose suspensions in glass tubes, embedded in a tank of 1% agarose. The estimated r_1 and r_2 relaxivities were 2.11 and $7.81 \text{ mM}^{-1} \text{ s}^{-1}$, respectively (Figure 12). As anticipated, r_1 increased with the decrease in field strength from 9.4 to 3.0 T, whereas r_2 decreased. This resulted in an estimated r_2/r_1 ratio of 3.70. The r_2/r_1 ratio is very similar to that achieved by Kim et al.⁸ with 2.2 nm maghemite nanoparticles and close to commercially available gadolinium-based contrast agents Magnevist (Gd-DTPA) and Gadovist (Gd-DO3A-butrol) with r_2/r_1 ratios of 1.41 and 1.42 at 3.0 T, respectively (Table 3). The low r_2 value of DMSA-ESCIoNs was due to their very small magnetic moment, influenced by the addition of Co^{2+} ions and small particle size. This minimized the magnetic induction of local magnetic field inhomogeneities and prevented DMSA-ESCIoNs from having a pronounced effect on T_2 relaxation. Particle concentration-dependent T_1 relaxation was achieved from the unpaired electrons of Co^{2+} and Fe^{3+} and the stability of the particles provided by the DMSA coating. These results demonstrate the potential of ESCIoNs for T_1 contrast enhancement for the first time.

3.5. Functionalization of DMSA-ESCIoNs and DMSA-ESIoNs with Bile Acid Ligand. DMSA-ESCIoNs have demonstrated potential as T_1 contrast imaging applications; however, their biocompatibility must be improved in order for clinical application to be successful. In addition to improving the biocompatibility of agents, design of target-specific agents to improve image resolution in specific biological regions is desired for early detection of disease. Hepatospecific MRI contrast agents are extremely useful for detecting focal liver lesions in the diagnosis of metastatic liver disease.⁷ Contrast

agents for detecting tissue abnormalities, however, must be able to cross the hepatocyte membrane and eventually be excreted via bile.⁶⁴ Bile acids, amphipathic molecules composed of a sterol scaffold with hydroxyl groups and a carboxyl-terminated side chain,³⁴ are transported to and from the liver via the enterohepatic circulation system and thus are ideal candidates for use as liver transport vehicles. Anelli et al.⁶⁵ tested whether cholic acid, cholyglycine, or cholytaurine linked to Gd-DOTA chelates could encourage hepatospecificity and found that cholic acid was an efficient carrier for uptake by hepatocytes.

With this in mind, we have explored the functionalization of cholic acid to DMSA-ESCIoNs and DMSA-ESIoNs for the first time as a step toward designing new liver-targeting nanoparticle MRI contrast agents. Both iron oxide and cobalt ferrite nanoparticles were synthesized for comparative purposes. To attach cholic acid to the particles, we first converted cholic acid into amino cholate by adaption of an existing protocol.³⁶ Chiefly, cholic acid was converted to *N*-hydroxysuccinimide ester using dicyclohexylcarbodiimide (DCC) as the coupling reagent. The activated ester was then transformed into cholate amide, which was reduced by LiAlH_4 to afford amino cholate. Nuclear magnetic resonance (NMR) studies were conducted to confirm the product of each step (see section 11 in the Supporting Information). The amino group of amino cholate was then conjugated to carboxylate groups on the surface of DMSA-ESCIoNs and DMSA-ESIoNs by EDC-NHS coupling. A schematic outlining the process of obtaining BA-ESCIoNs and BA-ESIoNs (BA, bile acid-functionalized) is shown in Figure 13.

To confirm conjugation of amino cholate to DMSA particles, FTIR was conducted. Figure 14 compares the FTIR spectra acquired for DMSA- and BA-functionalized ESCIoNs and ESIoNs. Following conjugation with bile acid, the broad peak at 3400 cm^{-1} (in the same region as OH stretching) sharpens due to NH stretching of the secondary amide group. Sharpening of the peaks at 2865 and 2930 cm^{-1} can be attributed to the symmetric and asymmetric CH_2 groups of amino cholate,⁶⁶ and the peak at 2970 cm^{-1} belongs to the asymmetric vibration of amino cholate's CH_3 groups. Additionally, the small peak at 1650 cm^{-1} is due to C=O amide stretching. The presence of NH and CH_3 stretching

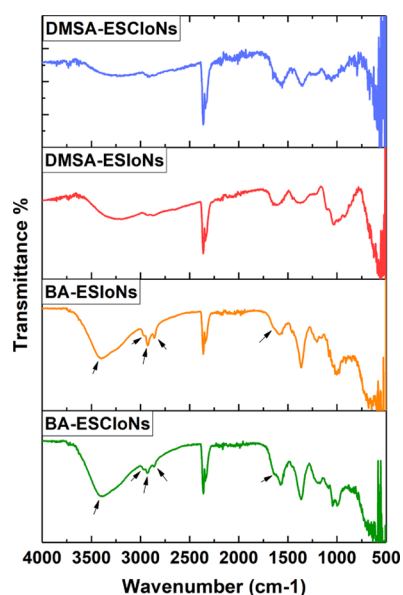


Figure 14. FTIR spectrum of DMSA- and BA-functionalized ESCIoNs and ESIOs.

peaks indicates conjugation of amino cholate to the DMSA-coated nanoparticles; further verification with the ninhydrin test can be found in section 12 in the Supporting Information.

Cryo-EM of BA-ESIOs and BA-ESCIoNs revealed networks of nanoparticles similar to that observed for DMSA-coated particles (Figure 15A,B). Although the appearance of the particles under cryo-EM was similar to that observed for

DMSA-ESIOs and ESCIoNs, noticeable sedimentation of the particles occurred after several days. To examine their stability, hydrodynamic diameter and zeta potential measurements were conducted in different pH levels. The average D_h 's for BA-ESIOs and BA-ESCIoNs at pH 7 were 476 ± 128 and 369 ± 74 nm, respectively. The significant increase in D_h indicates that particle aggregation has occurred after functionalization with bile acid. Bile acid is known to form helical aggregates due to its hydrophobic sterol backbone, which aids in transport to the liver.⁶⁷ Below pH 5, the D_h 's of both BA-ESIOs and BA-ESCIoNs increased, indicating that the particles are less stable in acidic conditions (Figure 15C). Zeta potential measurements mirror these results; ζ values of -36.5 ± 1.5 and -38.7 ± 1.0 mV were measured at pH 9 for Fe_3O_4 @BA and CoFe_2O_4 @BA nanoparticles, respectively (Figure 15D), whereas their ζ potentials at pH 3 increased to 19.1 ± 0.6 and -4.1 ± 0.2 mV.

To quantify the amount of bile acid on the surface of the nanoparticles, TGA measurements were performed. The weight loss profiles for BA-ESIOs and ESCIoNs were almost identical, with total weight losses of 45% (Figure S20). Considering that the weight loss for the same particles prior to bile acid functionalization was 36.4%, approximately 8.6% of the total weight loss is due to the bile acid ligands. Using eq 1, the number of bile acid ligands per ESCIoN particle was estimated to be 28. The approximate radius of a bile acid molecule is 3.5 \AA ,³⁰ and a single layer of DMSA is estimated to be 0.1 nm thick.⁶⁸ Thus, assuming a double layer of DMSA on a 2.4 nm core, the total surface area would be 24.6 nm^2 ,

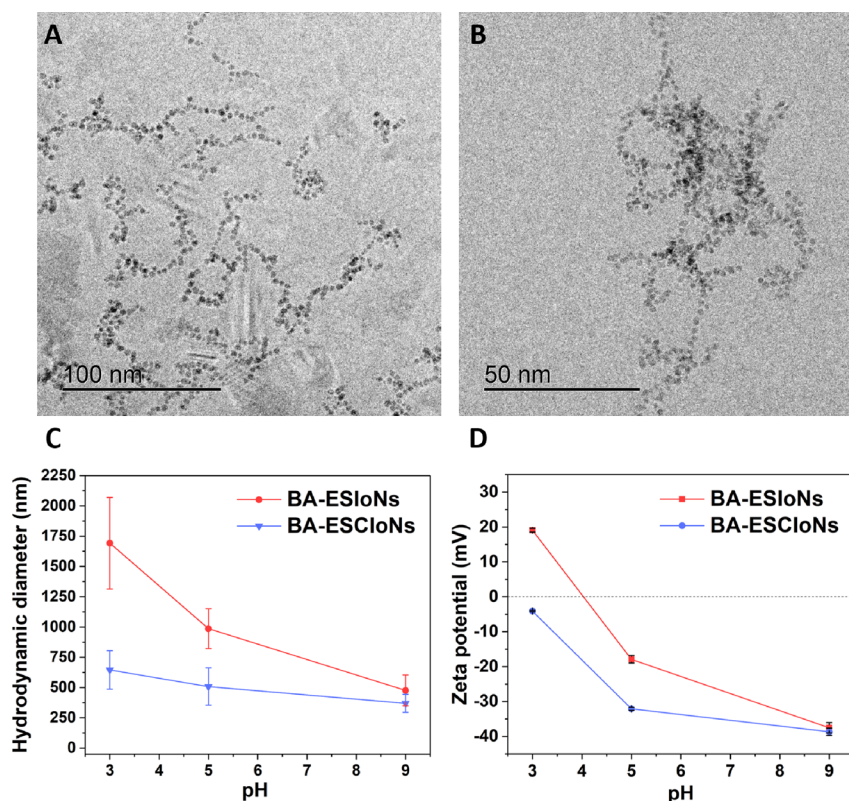


Figure 15. (A, B) Cryo-EM micrographs of (A) BA-ESIOs and (B) BA-ESCIoNs. (C) pH-dependent hydrodynamic measurements. (D) Zeta potential measurements showing that BA particles were stable in neutral and alkaline pH and that BA-ESIOs were less stable in acidic conditions than BA-ESCIoNs.

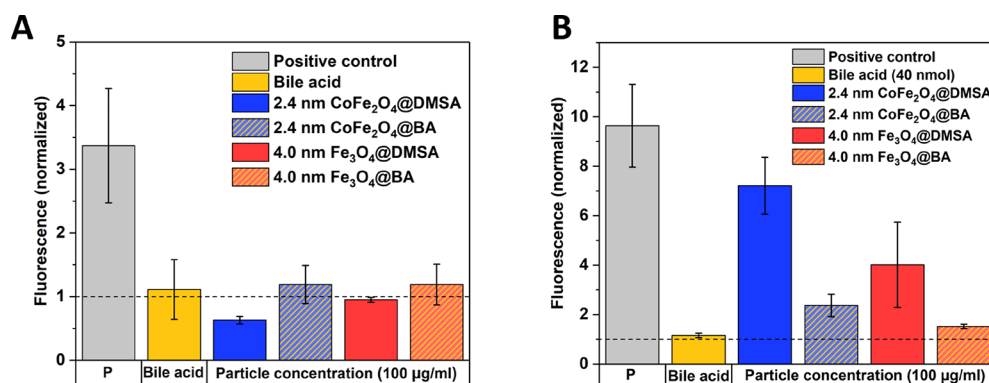


Figure 16. (A) Relative cell death (fluorescence) of HepG2 cells following exposure to DMSA- and BA-functionalized particles for 24 h. As controls for comparison, we used free bile acid and Triton X-100 (positive control). (B) Relative ROS production (fluorescence) of HepG2 cells following exposure to DMSA- and BA-functionalized particles for 24 h. Significant decrease in ROS production is observed following functionalization of DMSA-ESIOs and DMSA-ESCIos with a bile acid derivative. Fluorescence was normalized to a negative control (cell medium = 1) (positive control is hydrogen peroxide). Results are shown as mean \pm standard deviation from three independent experiments.

indicating that a single layer of bile acid is conjugated to the particle's surface.

Cytotoxic and oxidative stress effects of BA-ESCIos and BA-ESIOs toward HepG2 cells were assessed using the same protocol and conditions used previously for DMSA-coated particles. DMSA-ESCIos and ESIOs were re-evaluated conjunctively to determine any differences due to the presence of bile acid. Figure 16A shows that, at particle concentrations of 100 $\mu\text{g}/\text{mL}$, no cytotoxicity was observed with BA-ESCIos or BA-ESIOs. Figure 16B compares the ROS production for 2.4 and 4 nm particles capped with DMSA or DMSA and BA. Serendipitously, BA-ESCIos and BA-ESIOs significantly decreased the amount of ROS produced in comparison to DMSA-ESCIos or DMSA-ESIOs. The ROS production for CoFe₂O₄ nanoparticles decreased by approximately 67% when bile acid was conjugated to the nanoparticles. Similarly, the ROS production of Fe₃O₄ nanoparticles decreased by approximately 62%.

The reduction in ROS we observed suggests that bile acid acted as an ROS scavenger, mitigating oxidative stress effects. Bile acids have demonstrated antioxidant properties by directly intercepting peroxy radicals, as observed in a previous study.⁶⁹ Contrarily, hydrophobic bile acids can induce ROS production through disruption of the mitochondrial membrane.⁷⁰ The hydrophobicity of bile acids is linked to production of ROS, with deoxycholic acid (DCA) producing ROS, whereas hydrophilic ursodeoxycholic acid (UDCA) has antioxidant properties, which are especially relevant toward Fe³⁺-induced oxidative damage.⁷¹ UDCA was found to be an excellent scavenger of $\cdot\text{OH}$ radicals generated by FeCl₃-EDTA, as well as nonchelated Fe²⁺ and Fe³⁺ ions, preferentially interacting with Fe³⁺.⁷¹ Notably, the rate constant for the reaction was 10-fold higher than that of well-known pharmacological scavengers. Considering our findings and the order of bile acid hydrophilicity (UDCA < CA < CDCA < DCA < LCA),⁷² we propose that cholic acid shares similar antioxidant properties as UDCA and could be an effective site-specific ROS scavenger for free radicals induced by iron-containing nanoparticles. Further investigation to elucidate the mechanism of ROS scavenging by cholic acid is therefore warranted.

For liver-targeting biomedical applications, bile acid-functionalized nanoparticles could offer a convenient route to obtain biocompatible ferrite nanoparticles and mitigate their common issue of ROS generation. For potential application as

T₁ contrast agents, the magnetic properties of bile acid-functionalized nanoparticles should be evaluated, especially in consideration of their aggregation. The aggregation of bile acid functionalization could be addressed with further optimization of the conjugation process.

4. CONCLUSIONS

Extraordinarily small iron oxide and cobalt ferrite nanoparticles (ESIOs and ESCIOs, respectively) were synthesized with subnanometer-size precision using a simple thermal decomposition approach. Particle size was finely tuned by varying the oleylamine-to-precursor ratio, and ADF-STEM revealed their highly crystalline FCC spinel structure. Following ligand exchange with DMSA, the particles were stable in water for up to 12 months. DMSA-ESCIos and DMSA-ESIOs displayed superparamagnetic properties with a weak magnetic moment, owing to their small size and thus predominating effect of the magnetically disordered surface layer. Magnetic anisotropy introduced by Co²⁺ ions lowered the magnetic saturation for 2.4 nm ESCIOs, which proved effective for a diminishing effect on T₂ relaxation in MRI phantom studies. The resulting r₂/r₁ ratio of 3.70 at 3.0 T shows the potential of 2.4 nm ESCIOs as T₁-weighted MRI contrast agents for the first time. DMSA-ESCIos and ESIOs displayed no cytotoxic effects toward HepG2 cells; however, elevated levels of ROS were measured following a 24 h incubation period, particularly for DMSA-ESCIos. Following conjugation to amino cholate, a bile acid derivative, the ROS levels were, however, significantly reduced, indicating that amino cholate has the potential to act as an effective ROS scavenger for ferrite nanoparticle-induced free radicals. Bile acid-functionalized ESCIOs could offer a promising route for biocompatible liver-targeted MRI, and thus, further research into this area is encouraged.

■ ASSOCIATED CONTENT

Supporting Information

The Supporting Information is available free of charge on the ACS Publications website at DOI: 10.1021/acsami.8b17162.

List of chemicals and further information on the synthesis and ligand exchange of ESIOs and ESCIOs supported with TEM, XRD, cryo-EM, and SQUID measurements; calculations used to determine particle

concentrations; cytotoxicity and oxidative stress interference testing; NMR, TGA, and ninhydrin results for the synthesis of the bile acid derivative (PDF)

AUTHOR INFORMATION

Corresponding Author

*E-mail: dominique.piche@materials.ox.ac.uk.

ORCID

Dominique Piché: 0000-0001-7130-9150

Juan G. Lozano: 0000-0003-2900-3902

Lewys Jones: 0000-0002-6907-0731

Notes

The authors declare no competing financial interest.

ACKNOWLEDGMENTS

This research was supported by the Engineering and Physical Sciences Research Council (South of England Analytical Electron Microscope grant EP/K040375/1, DTA Fellowships Program (D.P.), and IAA block grants (N.G.)). We are also grateful for the financial support from Santander Academic Travel Awards (D.P.), Scatcherd European Scholarships (D.P.), the European Commission Seventh Framework Program (FP7-PEOPLE-ITN-2008-238363CONTACT), the Royal Society (N.G.), and the European Research Council (ERC-2009-StG-240500-DEDIGROWTH, ERC-2015-POC-680559-CONDUCT, ERC-2011-POC-309786-DEVICE, and ERC-2016-POC-754748-OxfordNano) (N.G.). The authors thank Rudolf Karos for the XRD measurements, Dr. Daniel Papp and Dr. Sebastian Rieger for the assistance with the 3.0 T MRI study, and Dr. Petra Herbeck-Engel for the FTIR measurements. We also thank Dr. Vitaliy Babenko for the development of the automated nanomaterials measurement software.

REFERENCES

- (1) McDonald, R. J.; McDonald, J. S.; Kallmes, D. F.; Jentoft, M. E.; Murray, D. L.; Thielen, K. R.; Williamson, E. E.; Eckel, L. J. Intracranial Gadolinium Deposition after Contrast-enhanced MR Imaging. *Radiology* **2015**, *275*, 772–782.
- (2) Gadolinium-Containing Contrast Agents: Removal of Omniscan and iv Magnevist, Restrictions to the Use of Other Linear Agents. <https://www.gov.uk/drug-safety-update/gadolinium-containing-contrast-agents-removal-of-omniscan-and-iv-magnevist-restrictions-to-the-use-of-other-linear-agents>.
- (3) Moore, F. G. A.; Levental, M. The Usefulness of Gadolinium-Enhanced Images on a Follow-up Magnetic Resonance Image in Suspected Multiple Sclerosis. *Can. Assoc. Radiol. J.* **2013**, *64*, 358–362.
- (4) Arami, H.; Khandhar, A.; Liggitt, D.; Krishnan, K. M. In Vivo Delivery, Pharmacokinetics, Biodistribution and Toxicity of Iron Oxide Nanoparticles. *Chem. Soc. Rev.* **2015**, *44*, 8576–8607.
- (5) Wang, Y. X. J.; Idee, J.-M. A Comprehensive Literature Update of Clinical Researches of Superparamagnetic Resonance Iron Oxide Nanoparticles for Magnetic Resonance Imaging. *Quant. Imaging Med. Surg.* **2017**, *7*, 88–122.
- (6) Chanyaputhipong, J.; Low, S.-C. A.; Chow, P. K. H. Gadoxetate Acid-Enhanced MR Imaging for HCC: A Review for Clinicians. *Int. J. Hepatol.* **2011**, 489342.
- (7) Albiin, N. MRI of Focal Liver Lesions. *Curr. Med. Imaging Rev.* **2012**, *8*, 107–116.
- (8) Kim, B. H.; Lee, N.; Kim, H.; An, K.; Park, Y. I.; Choi, Y.; Shin, K.; Lee, Y.; Kwon, S. G.; Na, H. B.; Park, J.-G.; Ahn, T.-Y.; Kim, Y.-W.; Moon, W. K.; Choi, S. H.; Hyeon, T. Large-Scale Synthesis of Uniform and Extremely Small-Sized Iron Oxide Nanoparticles for

High-Resolution T_1 Magnetic Resonance Imaging Contrast Agents. *J. Am. Chem. Soc.* **2011**, *133*, 12624–12631.

(9) Wei, H.; Bruns, O. T.; Kaul, M. G.; Hansen, E. C.; Barch, M.; Wisniowska, A.; Chen, O.; Chen, Y.; Li, N.; Okada, S.; Cordero, J. M.; Heine, M.; Farrar, C. T.; Montana, D. M.; Adam, G.; Ittrich, H.; Jasanoff, A.; Nielsen, P.; Bawendi, M. G. Exceedingly Small Iron Oxide Nanoparticles as Positive MRI Contrast Agents. *Proc. Natl. Acad. Sci.* **2017**, *114*, 2325–2330.

(10) Rui, Y.-P.; Liang, B.; Hu, F.; Xu, J.; Peng, Y.-F.; Yin, P.-H.; Duan, Y.; Zhang, C.; Gu, H. Ultra-Large-Scale Production of Ultrasmall Superparamagnetic Iron Oxide Nanoparticles for T_1 -Weighted MRI. *RSC Adv.* **2016**, *6*, 22575–22585.

(11) Zhang, H.; Li, L.; Liu, X. L.; Jiao, J.; Ng, C.-T.; Yi, J. B.; Luo, Y. E.; Bay, B.-H.; Zhao, L. Y.; Peng, M. L.; Gu, N.; Fan, H. M. Ultrasmall Ferrite Nanoparticles Synthesized via Dynamic Simultaneous Thermal Decomposition for High-Performance and Multifunctional T_1 Magnetic Resonance Imaging Contrast Agent. *ACS Nano* **2017**, *11*, 3614–3631.

(12) Singh, N.; Jenkins, G. J. S.; Asadi, R.; Doak, S. H. Potential Toxicity of Superparamagnetic Iron Oxide Nanoparticles (SPION). *Nano Rev.* **2010**, *1*, 5358.

(13) Finetti, F.; Terzuoli, E.; Donnini, S.; Uva, M.; Ziche, M.; Morbidelli, L. Monitoring Endothelial and Tissue Responses to Cobalt Ferrite Nanoparticles and Hybrid Hydrogels. *PLoS ONE* **2016**, *11*, No. e0168727.

(14) Galarreta, I.; Insausti, M.; Gil de Muro, I.; Ruiz de Larramendi, I.; Lezama, L. Exploring Reaction Conditions to Improve the Magnetic Response of Cobalt-Doped Ferrite Nanoparticles. *Nano-materials* **2018**, *8*, 63.

(15) Volatron, J.; Kolosnjaj-Tabi, J.; Javed, Y.; Vuong, Q. L.; Gossuin, Y.; Neveu, S.; Luciani, N.; Hémedi, M.; Carn, F.; Alloyeau, D.; Gazeau, F. Physiological Remediation of Cobalt Ferrite Nanoparticles by Ferritin. *Sci. Rep.* **2017**, *7*, 40075.

(16) Joshi, H. M.; Lin, Y. P.; Aslam, M.; Prasad, P. V.; Schultz-Sikma, E. A.; Edelman, R.; Meade, T.; Dravid, V. P. Effects of Shape and Size of Cobalt Ferrite Nanostructures on Their MRI Contrast and Thermal Activation. *J. Phys. Chem., C* **2009**, *113*, 17761–17767.

(17) Mazario, E.; Menéndez, N.; Herrasti, P.; Cañete, M.; Connord, V.; Carrey, J. Magnetic Hyperthermia Properties of Electrosynthesized Cobalt Ferrite Nanoparticles. *J. Phys. Chem., C* **2013**, *117*, 11405–11411.

(18) Mohapatra, J.; Mitra, A.; Bahadur, D.; Aslam, M. Surface Controlled Synthesis of MFe_2O_4 ($M = Mn, Fe, Co, Ni$ and Zn) Nanoparticles and Their Magnetic Characteristics. *CrystEngComm* **2013**, *15*, 524–532.

(19) Liu, F.; Laurent, S.; Fattahi, H.; Vander Elst, L.; Muller, R. N. Superparamagnetic Nanosystems Based on Iron Oxide Nanoparticles for Biomedical Imaging. *Nanomedicine* **2011**, *6*, 519–528.

(20) Kucheryavy, P.; He, J.; John, V. T.; Maharjan, P.; Spinu, L.; Goloverda, G. Z.; Kolesnichenko, V. L. Superparamagnetic Iron Oxide Nanoparticles with Variable Size and an Iron Oxidation State as Prospective Imaging Agents. *Langmuir* **2013**, *29*, 710–716.

(21) Park, J.; Lee, E.; Hwang, N.-M.; Kang, M.; Kim, S. C.; Hwang, Y.; Park, J.-G.; Noh, H.-J.; Kim, J.-Y.; Park, J.-H.; Hyeon, T. One-Nanometer-Scale Size-Controlled Synthesis of Monodisperse Magnetic Iron Oxide Nanoparticles. *Angew. Chem., Int. Ed.* **2005**, *44*, 2872–2877.

(22) Zhu, Y.; Jiang, F. Y.; Chen, K.; Kang, F.; Tang, Z. K. Size-Controlled Synthesis of Monodisperse Superparamagnetic Iron Oxide Nanoparticles. *J. Alloys Compd.* **2011**, *509*, 8549–8553.

(23) Sun, S.; Zeng, H.; Robinson, D. B.; Raoux, S.; Rice, P. M.; Wang, S. X.; Li, G. Monodisperse MFe_2O_4 ($M = Fe, Co, Mn$) Nanoparticles. *J. Am. Chem. Soc.* **2004**, *126*, 273–279.

(24) Xie, J.; Peng, S.; Brower, N.; Pourmand, N.; Wang, S. X.; Sun, S. One-Pot Synthesis of Monodisperse Iron Oxide Nanoparticles for Potential Biomedical Applications. *Pure Appl. Chem.* **2006**, *78*, 1003–1014.

(25) Yu, Y.; Yang, W.; Sun, X.; Zhu, W.; Li, X.-Z.; Sellmyer, D. J.; Sun, S. Monodisperse MPt ($M = Fe, Co, Ni, Cu, Zn$) Nanoparticles

Prepared from a Facile Oleylamine Reduction of Metal Salts. *Nano Lett.* **2014**, *14*, 2778–2782.

(26) Lu, L. T.; Dung, N. T.; Tung, L. D.; Thanh, C. T.; Quy, O. K.; Chuc, N. V.; Maenosono, S.; Thanh, N. T. K. Synthesis of Magnetic Cobalt Ferrite Nanoparticles with Controlled Morphology, Monodispersity and Composition: The Influence of Solvent, Surfactant, Reductant and Synthetic Conditions. *Nanoscale* **2015**, *7*, 19596–19610.

(27) Georgiadou, V.; Kokotidou, C.; Le Droumaguet, B.; Carbonnier, B.; Choli-Papadopoulou, T.; Dendrinou-Samara, C. Oleylamine as a Beneficial Agent for the Synthesis of CoFe_2O_4 Nanoparticles with Potential Biomedical Uses. *Dalton Trans.* **2014**, *43*, 6377–6388.

(28) Fauconnier, N.; Pons, J. N.; Roger, J.; Bee, A. Thiolation of Maghemite Nanoparticles by Dimercaptosuccinic Acid. *J. Colloid Interface Sci.* **1997**, *194*, 427–433.

(29) Palma, S. I. C. J.; Marciello, M.; Carvalho, A.; Veintemillas-Verdaguer, S.; Morales, M. d. P.; Roque, A. C. A. Effects of Phase Transfer Ligands on Monodisperse Iron Oxide Magnetic Nanoparticles. *J. Colloid Interface Sci.* **2015**, *437*, 147–155.

(30) Monte, M. J.; Marin, J. J.; Antelo, A.; Vazquez-Tato, J. Bile Acids: Chemistry, Physiology, and Pathophysiology. *World J. Gastroenterol.* **2009**, *15*, 804–816.

(31) Kramer, W.; Wess, G.; Schubert, G.; Bickel, M.; Girbig, F.; Gutjahr, U.; Kowalewski, S.; Baringhaus, K. H.; Enhsen, A.; Glombik, H. Liver-Specific Drug Targeting by Coupling to Bile Acids. *J. Biol. Chem.* **1992**, *267*, 18598–18604.

(32) Zhang, Z.; Cai, H.; Liu, Z.; Yao, P. Effective Enhancement of Hypoglycemic Effect of Insulin by Liver-Targeted Nanoparticles Containing Cholic Acid-Modified Chitosan Derivative. *Mol. Pharmaceutics* **2016**, *13*, 2433–2442.

(33) Chong, H.-S.; Song, H. A.; Lim, S.; Macrenaris, K.; Ma, X.; Lee, H.; Bui, P.; Meade, T. A Novel Cholic Acid-Based Contrast Enhancement Agent for Targeted MRI. *Bioorg. Med. Chem. Lett.* **2008**, *18*, 2505–2508.

(34) Assfalg, M.; Gianolio, E.; Zanzoni, S.; Tomaselli, S.; Russo, V. L.; Cabella, C.; Ragona, L.; Aime, S.; Molinari, H. NMR Structural Studies of the Supramolecular Adducts between a Liver Cytosolic Bile Acid Binding Protein and Gadolinium(III)-Chelates Bearing Bile Acids Residues: Molecular Determinants of the Binding of a Hepatospecific Magnetic Resonance Imaging Contrast Agent. *J. Med. Chem.* **2007**, *50*, 5257–5268.

(35) Ivask, A.; Titma, T.; Visnapuu, M.; Vija, H.; Kakinen, A.; Sihtmae, M.; Pokhrel, S.; Madler, L.; Heinlaan, M.; Kisand, V.; Shimmo, R.; Kahru, A. Toxicity of 11 Metal Oxide Nanoparticles to Three Mammalian Cell Types In Vitro. *Curr. Top. Med. Chem.* **2015**, *15*, 1914–1929.

(36) Zhou, Y.; Ryu, E.-H.; Zhao, Y.; Woo, L. K. Solvent-Responsive Metalloporphyrins: Binding and Catalysis. *Organometallics* **2007**, *26*, 358–364.

(37) Xu, Z.; Shen, C.; Hou, Y.; Gao, H.; Sun, S. Oleylamine as Both Reducing Agent and Stabilizer in a Facile Synthesis of Magnetite Nanoparticles. *Chem. Mater.* **2009**, *21*, 1778–1780.

(38) Jones, L.; Yang, H.; Pennycook, T. J.; Marshall, M. S. J.; Van Aert, S.; Browning, N. D.; Castell, M. R.; Nellist, P. D. Smart Align—A New Tool for Robust Non-Rigid Registration of Scanning Microscope Data. *Adv. Struct. Chem. Imaging* **2015**, *1*, 1–16.

(39) Colliex, C.; Manoubi, T.; Ortiz, C. Electron-Energy-Loss-Spectroscopy Near-Edge Fine Structures in the Iron-Oxygen System. *Phys. Rev. B* **1991**, *44*, 11402–11411.

(40) Rez, P. Cross-Sections for Energy Loss Spectrometry. *Ultramicroscopy* **1982**, *9*, 283–287.

(41) Schmid, H. K.; Mader, W. Oxidation States of Mn and Fe in Various Compound Oxide Systems. *Micron* **2006**, *37*, 426–432.

(42) Almeida, T. P.; Kasama, T.; Muxworthy, A. R.; Williams, W.; Nagy, L.; Hansen, T. W.; Brown, P. D.; Dunin-Borkowski, R. E. Visualized Effect of Oxidation on Magnetic Recording Fidelity in Pseudo-Single-Domain Magnetite Particles. *Nat. Commun.* **2014**, *5*, 5154.

(43) Pedrosa, J.; Costa, B. F. O.; Portugal, A.; Duraes, L. Controlled Phase Formation of Nanocrystalline Iron Oxides/Hydroxides in Solution – An Insight on the Phase Transformation Mechanisms. *Mater. Chem. Phys.* **2015**, *163*, 88–98.

(44) Ta, H. T.; Li, Z.; Wu, Y.; Cowin, G.; Zhang, S.; Yago, A.; Whittaker, A. K.; Xu, Z. P. Effects of Magnetic Field Strength and Particle Aggregation on Relaxivity of Ultra-Small Dual Contrast Iron Oxide Nanoparticles. *Mater. Res. Express* **2017**, *4*, 116105.

(45) Soenen, S. J.; Rivera-Gil, P.; Montenegro, J.-M.; Parak, W. J.; De Smedt, S. C.; Braeckmans, K. Cellular Toxicity of Inorganic Nanoparticles: Common Aspects and Guidelines for Improved Nanotoxicity Evaluation. *Nano Today* **2011**, *6*, 446–465.

(46) Chen, Z. P.; Zhang, Y.; Zhang, S.; Xia, J. G.; Liu, J. W.; Xu, K.; Gu, N. Preparation and Characterization of Water-Soluble Monodisperse Magnetic Iron Oxide Nanoparticles Via Surface Double-Exchange with DMSA. *Colloids Surf., A* **2008**, *316*, 210–216.

(47) Lim, J.; Yeap, S. P.; Che, H. X.; Low, S. C. Characterization of Magnetic Nanoparticle by Dynamic Light Scattering. *Nanoscale Res. Lett.* **2013**, *8*, 381.

(48) Qi, M.; Zhang, K.; Li, S.; Wu, J.; Pham-Huy, C.; Diao, X.; Xiao, D.; He, H. Superparamagnetic Fe_3O_4 Nanoparticles: Synthesis by a Solvothermal Process and Functionalization for a Magnetic Targeted Curcumin Delivery System. *New J. Chem.* **2016**, *40*, 4480–4491.

(49) Pino, P. d.; Pelaz, B.; Zhang, Q.; Maffre, P.; Nienhaus, G. U.; Parak, W. J. Protein Corona Formation Around Nanoparticles – From the Past to the Future. *Mater. Horiz.* **2014**, *1*, 301–313.

(50) Noori, A.; Parivar, K.; Modaresi, M.; Messripour, M.; Yousefi, M. H.; Amiri, G. R. Effect of Magnetic Iron Oxide Nanoparticles on Pregnancy and Testicular Development of Mice. *Afr. J. Biotechnol.* **2011**, *10*, 1221–1227.

(51) Vestal, C. R.; Zhang, Z. J. Effects of Surface Coordination Chemistry on the Magnetic Properties of MnFe_2O_4 Spinel Ferrite Nanoparticles. *J. Am. Chem. Soc.* **2003**, *125*, 9828–9833.

(52) Peddis, D.; Mansilla, M. V.; Morup, S.; Cannas, C.; Musinu, A.; Piccaluga, G.; D'Orazio, F.; Lucari, F.; Fiorani, D. Spin-Canting and Magnetic Anisotropy in Ultrasmall CoFe_2O_4 Nanoparticles. *J. Phys. Chem. B* **2008**, *112*, 8507–8513.

(53) Fu, P. P.; Xia, Q.; Hwang, H.-M.; Ray, P. C.; Yu, H. Mechanisms of Nanotoxicity: Generation of Reactive Oxygen Species. *J. Food Drug Anal.* **2014**, *22*, 64–75.

(54) Klein, S.; Kizaloglu, M.; Portilla, L.; Park, H.; Rejek, T.; Hummer, J.; Meyer, K.; Hock, R.; Distel, L. V. R.; Halik, M.; Kryschi, C. Enhanced In Vitro Biocompatibility and Water Dispersibility of Magnetite and Cobalt Ferrite Nanoparticles Employed as ROS Formation Enhancer in Radiation Cancer Therapy. *Small* **2018**, *14*, 1704111.

(55) Winterbourn, C. C. Toxicity of Iron and Hydrogen Peroxide: The Fenton Reaction. *Toxicol. Lett.* **1995**, *82*-83, 969–974.

(56) Chumakov, A.; Batalova, V.; Slizhov, Y. Electro-Fenton-Like Reactions of Transition Metal Ions with Electrogenerated Hydrogen Peroxide. *AIP Conf. Proc.* **2016**, *1772*, No. 040004.

(57) Porwol, T.; Ehleben, W.; Zierold, K.; Fandrey, J.; Acker, H. The Influence of Nickel and Cobalt on Putative Members of the Oxygen-Sensing Pathway of Erythropoietin-Producing HepG2 Cells. *Eur. J. Biochem.* **1998**, *256*, 16–23.

(58) Horev-Azaria, L.; Baldi, G.; Beno, D.; Bonacchi, D.; Golla-Schindler, U.; Kirkpatrick, J. C.; Kolle, S.; Landsiedel, R.; Maimon, O.; Marche, P. N.; Ponti, J.; Romano, R.; Rossi, F.; Sommer, D.; Uboldi, C.; Unger, R. E.; Villiers, C.; Korenstein, R. Predictive Toxicology of Cobalt Ferrite Nanoparticles: Comparative in-Vitro Study of Different Cellular Models Using Methods of Knowledge Discovery from Data. *Part. Fibre Toxicol.* **2013**, *10*, 32.

(59) Ghasemian, Z.; Shahbazi-Gahrouei, D.; Manouchehri, S. Cobalt Zinc Ferrite Nanoparticles as a Potential Magnetic Resonance Imaging Agent: An In vitro Study. *Avicenna J. Med. Biotechnol.* **2015**, *7*, 64–68.

(60) Nidhin, M.; Nazeer, S. S.; Jayasree, R. S.; Kiran, M. S.; Nair, B. U.; Sreeram, K. J. Flower Shaped Assembly of Cobalt Ferrite

Nanoparticles: Application as T_2 Contrast Agent in MRI. *RSC Adv.* **2013**, *3*, 6906–6912.

(61) Rohrer, M.; Bauer, H.; Mintorovitch, J.; Requardt, M.; Weinmann, H.-J. Comparison of Magnetic Properties of MRI Contrast Media Solutions at Different Magnetic Field Strengths. *Invest. Radiol.* **2005**, *40*, 715–724.

(62) Kovár, D.; Malá, A.; Mlčochová, J.; Kalina, M.; Fohlerová, Z.; Hlaváček, A.; Farka, Z.; Skládal, P.; Starčuk, Z.; Jiřík, R.; Slabý, O.; Hubálek, J. Preparation and Characterisation of Highly Stable Iron Oxide Nanoparticles for Magnetic Resonance Imaging. *J. Nanomater.* **2017**, *2017*, 7859289.

(63) Jedlovszky-Hajdu, A.; Tombacz, E.; Banyai, I.; Babos, M.; Palko, A. Carboxylated Magnetic Nanoparticles as MRI Contrast Agents: Relaxation Measurements at Different Field Strengths. *J. Magn. Magn. Mater.* **2012**, *324*, 3173–3180.

(64) Betebenner, D. A.; Carney, P. L.; Zimmer, A. M.; Kazikiewicz, J. M.; Brucher, E.; Sherry, A. D.; Johnson, D. K. Hepatobiliary Delivery of Polyaminopolycarboxylate Chelates: Synthesis and Characterization of a Cholic Acid Conjugate of EDTA and Biodistribution and Imaging Studies with Its Indium-111 Chelate. *Bioconjugate Chem.* **1991**, *2*, 117–123.

(65) Anelli, P. L.; Lattuada, L.; Lorusso, V.; Lux, G.; Morisetti, A.; Morosini, P.; Serletti, M.; Uggeri, F. Conjugates of Gadolinium Complexes to Bile Acids as Hepatocyte-Directed Contrast Agents for Magnetic Resonance Imaging. *J. Med. Chem.* **2004**, *47*, 3629–3641.

(66) Mendelsohn, R.; Flach, C. R.; Moore, D. J. Determination of Molecular Conformation and Permeation in Skin via IR Spectroscopy, Microscopy, and Imaging. *Biochim. Biophys. Acta, Biomembr.* **2006**, *1758*, 923–933.

(67) Babu, P.; Sangeetha, N. M.; Maitra, U. Supramolecular Chemistry of Bile Acid Derivatives: Formation of Gels. *Macromol. Symp.* **2006**, *241*, 60–67.

(68) Eriksson, P. A New Synthesis of Nanoparticles Designed for Biomedical Imaging. A Pilot Study. Dissertation, Linköping University, 2013.

(69) DeLange, R. J.; Glazer, A. N. Bile Acids: Antioxidants or Enhancers of Peroxidation Depending on Lipid Concentration. *Arch. Biochem. Biophys.* **1990**, *276*, 19–25.

(70) Fang, Y.; Han, S. I.; Mitchell, C.; Gupta, S.; Studer, E.; Grant, S.; Hylemon, P. B.; Dent, P. Bile Acids Induce Mitochondrial ROS Which Promote Activation of Receptor Tyrosine Kinases and Signaling Pathways in Rat Hepatocytes. *Hepatology* **2004**, *40*, 961–971.

(71) Lapenna, D.; Ciofani, G.; Festi, D.; Neri, M.; Pierdomenico, S. D.; Giamberardino, M. A.; Cuccurullo, F. Antioxidant Properties of Ursodeoxycholic Acid. *Biochem. Pharmacol.* **2002**, *64*, 1661–1667.

(72) Perez, M. J.; Briz, O. Bile-Acid-Induced Cell Injury and Protection. *World J. Gastroenterol.* **2009**, *15*, 1677–1689.